MICROBIOLOGY

Inhibition of microbial deconjugation of micellar bile acids protects against intestinal permeability and liver injury

Darrick K. Li[1]†‡, Snehal N. Chaudhari[2]†, Yoojin Lee[1], Mozhdeh Sojoodi[3], Arijit A. Adhikari[2], Lawrence Zukerberg[4], Stuti Shroff[4], Stephen Cole Barrett[3], Kenneth Tanabe[3], Raymond T. Chung[1]*, A. Sloan Devlin[2]*

Altered host-microbe interactions and increased intestinal permeability have been implicated in disease pathogenesis. However, the mechanisms by which intestinal microbes affect epithelial barrier integrity remain unclear. Here, we investigate the impact of bacterial metabolism of host-produced bile acid (BA) metabolites on epithelial barrier integrity. We observe that rats fed a choline-deficient, L-amino acid–defined, high-fat diet (CDAHFD) exhibit reduced intestinal abundance of host-produced conjugated BAs at early time points, coinciding with increased gut permeability. We show that in vitro, conjugated BAs protect gut epithelial monolayers from damage caused by bacterially produced unconjugated BAs through micelle formation. We then demonstrate that inhibition of bacterial BA deconjugation with a small-molecule inhibitor prevents the development of pathologic intestinal permeability and hepatic inflammation in CDAHFD-fed rats. Our study identifies a signaling-independent, physicochemical mechanism for conjugated BA-mediated protection of epithelial barrier function and suggests that rational manipulation of microbial BA metabolism could be leveraged to regulate gut barrier integrity.

INTRODUCTION

In health, the intestinal epithelium forms a dynamic and tightly sealed barrier that is selectively permeable (*1*). However, under pathologic conditions, tight junctions can become disrupted with excessive leakage of dietary and bacterial antigens, including lipopolysaccharide (LPS), into portal and systemic circulation, directly inducing inflammation in extraintestinal organs (*2*). Emerging data have implicated increased intestinal permeability in the pathogenesis of a range of human diseases, including inflammatory bowel disease, liver disease, type 1 and type 2 diabetes, cardiovascular disease, and depression (*3*–*7*). The gut microbial communities of these patients are altered compared to healthy individuals, and gut microbial imbalance has been proposed to contribute to the development of intestinal permeability (*8*, *9*). However, the specific host and microbial factors that result in the development of pathologic intestinal permeability remain unclear.

Bile acids (BAs) have been implicated as potential causal agents in the development of pathogenic intestinal permeability (*10*, *11*). BAs are steroidal natural products that are present in high concentrations in the gut (~200 μM to 1 mM in the large intestine) (*12*). In the liver, host enzymes convert cholesterol into conjugated primary BAs, which contain a steroidal core appended to taurine or glycine through an amide bond linkage (Fig. 1A). These compounds act as digestive surfactants; in humans, these metabolites are stored in the gallbladder and secreted into the small intestine postprandially to aid in the absorption of lipids and vitamins (*13*). In the lower gastrointestinal tract, bacteria convert primary conjugated BAs into unconjugated primary BAs through the action of bile salt hydrolase (BSH) enzymes (*14*). BSHs are expressed in a broad range of human gut bacteria (*15*) and have no mammalian homolog (*16*). Bacterial enzymes then further chemically modify primary BAs, producing unconjugated secondary BAs. Following enterohepatic recirculation, these molecules can be converted to conjugated primary and secondary BAs in the liver and then resecreted into the gut (*14*).

Studies have demonstrated that individual BAs bind directly to host receptors at submicromolar concentrations to activate signaling pathways and that altered BA populations can lead to metabolic derangements (*13*, *17*). However, the pathological roles of micellar concentrations of BAs, as they exist in physiologically relevant systems, remain underexplored. Particularly in the intestine, BAs exist in millimolar concentrations capable of affecting nutrient absorption, fat solubilization, and membrane permeabilization (*18*). Previous work has demonstrated that exposure of epithelial monolayers to certain hydrophobic BAs, including unconjugated BAs, leads to increased intestinal permeability and may contribute to the development of intestinal inflammation and disruption of intestinal homeostasis (*19*, *20*). In animal models, long-term administration of a high-fat diet (HFD) has been shown to lead to increased intestinal permeability associated with an enrichment of hydrophobic BAs in the intestinal BA pool (*21*–*23*). While unconjugated BAs increase epithelial permeability, the role of conjugated BAs in epithelial permeability is unclear. Moreover, it is not known whether bacterial BA deconjugation affects intestinal homeostasis. Last, whether the detergent roles of BAs affect intestinal permeability at the onset of disease has not been explored.

Considering the close physiological relationship between the gut and the liver, intestinal barrier function is crucial for liver homeostasis, and disruption of intestinal barrier integrity may accelerate

[1]Liver Center, Massachusetts General Hospital, Harvard Medical School, Boston, MA, USA. [2]Department of Biological Chemistry and Molecular Pharmacology, Blavatnik Institute, Harvard Medical School, Boston, MA, USA. [3]Department of Surgery, Massachusetts General Hospital, Harvard Medical School, Boston, MA, USA. [4]Department of Pathology, Massachusetts General Hospital, Harvard Medical School, Boston, MA, USA.
*Corresponding author. Email: sloan_devlin@hms.harvard.edu (A.S.D.); chung.raymond@mgh.harvard.edu (R.T.C.)
†These authors contributed equally to this work as co-first authors.
‡Present address: Section of Digestive Diseases, Department of Medicine, Yale School of Medicine, New Haven, CT, USA.

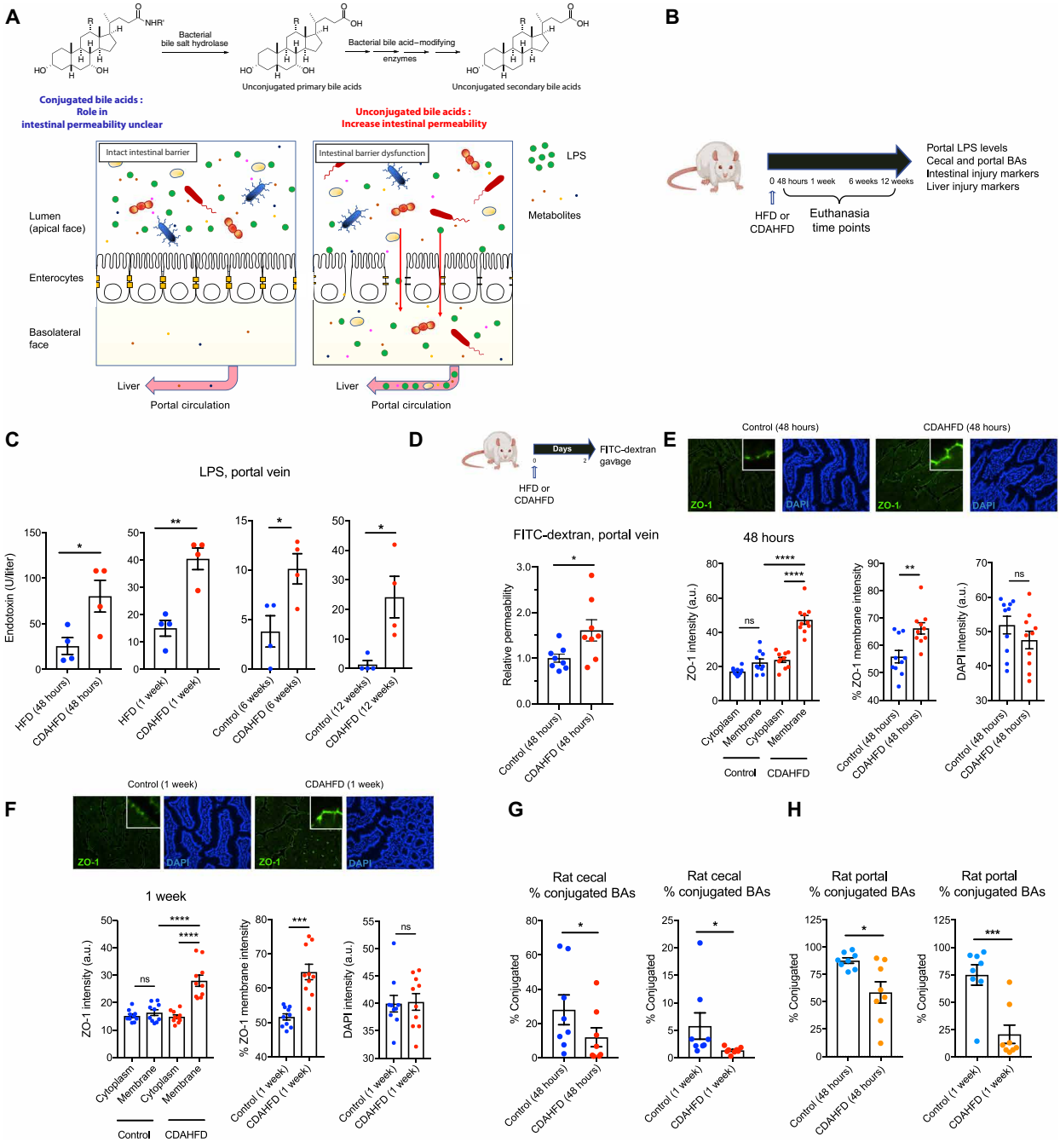

Fig. 1. CDAHFD-fed rats develop increased intestinal permeability at early time points coinciding with decreased conjugated BA abundance. (**A**) Human gut bacterial enzymes transform conjugated primary BAs into unconjugated secondary BAs. While hydrophilic unconjugated BAs damage epithelial integrity, the roles of unconjugated BAs and bacterial BSHs in intestinal membrane integrity are unclear. (**B**) Schematic of rat intestinal permeability time-course experiment. A choline-deficient, L-amino acid defined (CDAHFD) was fed to rats to induce intestinal permeability and liver damage. HFD-fed rats served as controls. Rats were euthanized at 48-hour, 1-week, 6-week, or 12-week time points. Tissues and blood were collected for metabolite quantification and evaluation of intestinal and liver injury markers. (**C**) Portal venous levels of LPS were significantly increased in CDAHFD-fed rats compared to control rats after 48 hours, 1 week, 6 weeks, and 12 weeks on diet ($n = 4$ per group, two-tailed Welch's t test). (**D**) CDAHFD-fed rats developed increased intestinal permeability after 48 hours of diet. Measurement of fluorescein isothiocyanate (FITC)–dextran levels in systemic circulation after gavage in control and CDAHFD-fed rats ($n = 8$ per group, two-tailed Welch's t test). (**E** and **F**) CDAHFD induced increased expression and apical membrane localization of ZO-1 at early time points. ZO-1 immunofluorescence staining of ileum from control and CDAHFD-fed rats at 48-hour (E) and 1-week (F) time points ($n = 10$ intestinal cells quantified per group; see Materials and Methods for statistical analyses). (**G** and **H**) Conjugated BA abundance was reduced at early time points (48 hours and 1 week) in the cecum (G) and portal vein (H) of CDAHFD-fed rats as determined by ultra-performance liquid chromatography–mass spectrometry (UPLC-MS) BA analysis from control and CDAHFD-fed animals ($n = 8$ per group, two-tailed Welch's t test; see the Supplementary Materials for concentrations of total and individual BAs in cecal contents and portal vein at 48 hours and 1 week). See Materials and Methods for statistical analyses. $^*P < 0.05$, $^{**}P < 0.005$, $^{***}P < 0.001$, and $^{****}P < 0.0001$. Bars represent means ± SEM. ns, not significant; DAPI, 4′,6-diamidino-2-phenylindole; a.u., arbitrary units.

the pathogenesis of liver disease (*4*, *24*). To investigate how BAs affect intestinal permeability, we used a rodent model of diet-induced liver disease (*25*). We observe that increased small intestine permeability is an early feature of liver disease in rats fed a choline-deficient, L-amino acid–defined, HFD (CDAHFD). We also observed a significant reduction in the abundance of intestinal and portal venous conjugated BAs in CDAHFD-treated rats at early time points. Hypothesizing that conjugated BAs could protect the intestinal barrier against chemical insults, we demonstrate that tauro-conjugated BAs sequester unconjugated BAs into micelles. We then show that this physicochemical sequestration of unconjugated BAs protects epithelial cells from damage and permeability in vitro, thus providing a signaling-independent role for micellar BAs in maintaining gut barrier integrity. Furthermore, using a small-molecule inhibitor of bacterial BSHs that we recently developed (*26*, *27*), we show that inhibition of BSH activity increases conjugated BA abundance and prevents the development of increased small intestine permeability, hepatic steatosis, and hepatic inflammation in diseased rats. Last, we demonstrate that glyco-conjugated BAs, the predominant BAs in humans, also protect against epithelial damage caused by unconjugated BAs in vitro. Together, these data indicate that gut microbial enzymes interact with host metabolites to affect intestinal barrier function.

RESULTS

CDAHFD-fed rats develop increased intestinal permeability before developing hepatic inflammation

To investigate the molecular mechanisms leading to the development of intestinal permeability in the context of an animal model relevant to human disease, we used a CDAHFD in rats. CDAHFD is an established rodent model of diet-induced cirrhosis that is characterized by disrupted epithelial barrier integrity (*28*). Previous studies have also found choline deficiency to be associated with the development of nonalcoholic fatty liver disease (NAFLD) and nonalcoholic steatohepatitis (NASH) in humans (*29*, *30*). CDAHFD-fed rats developed cirrhosis in 12 weeks (*31*), while controls fed a HFD with equivalent fat by weight developed microvesicular steatosis without inflammation or fibrosis (fig. S1A). CDAHFD-fed rats gained less weight than controls and exhibited significantly increased markers of hepatocellular injury, hepatic hydroxyproline levels, and mRNA expression of fibrosis-related and inflammatory genes at 12 weeks after diet intervention [fig. S1, B and C; refer to table S1 for all quantitative polymerase chain reaction (qPCR) primer sequences].

To assess intestinal permeability, we measured the portal LPS in CDAHFD-fed rats at 48 hours, 1 week, 6 weeks, and 12 weeks (Fig. 1, A and B). Portal LPS levels were higher in CDAHFD-fed rats compared to controls as early as 48 hours after diet intervention (Fig. 1C), when markers of liver injury were not yet significantly elevated (fig. S1, C to E). Further, intestinal epithelium from CDAHFD-fed rats exhibited significantly increased inflammation and epithelial hyperplasia at early time points (fig. S1F). These data suggest that intestinal injury and permeability precede hepatic phenotypes in the CDAHFD model of liver disease. To confirm these results, using a fluorescein isothiocyanate (FITC)–dextran assay, we found that CDAHFD-fed rats exhibited a significant increase in intestinal permeability compared to controls at 48 hours after diet initiation (Fig. 1D). We observed significantly increased membrane localization of zonula occludens-1 (ZO-1) in intestinal epithelial cells from the ileum of CDAHFD-fed rats at 48 hours that persisted after 1 week of diet (Fig. 1, E and F). Increased expression and plasma membrane localization of ZO-1 are indicative of increased intestinal permeability (*32*, *33*). Moreover, treatment of gut epithelial cells with permeability agents results in dynamic changes in ZO-1 subcellular localization, including recruitment to the plasma membrane (*34*, *35*). Hence, ZO-1 redistribution in the small intestinal epithelium of CDAHFD-fed rats is consistent with increased intestinal permeability. At 48 hours, CDAHFD-fed rats did not exhibit any evidence of hepatic inflammation compared to controls, while inflammation was apparent at 1 week after dietary intervention (fig. S1, C to E). Together, these results demonstrate that small intestine permeability is an early feature of this animal model and precedes the development of hepatic inflammation.

Conjugated BAs are reduced in the cecum and portal veins of CDAHFD-fed rats at early time points

To assess whether changes in BAs are associated with increased intestinal permeability, we performed intestinal and portal venous BA profiling in CDAHFD-fed and control rats using ultra-performance liquid chromatography–mass spectrometry (UPLC-MS). We observed a significant decrease in the abundance of cecal and portal venous conjugated BAs in CDAHFD-fed rats at 48 hours and 1 week after dietary intervention (Fig. 1, G and H). In particular, levels of tauro-cholic acid (TCA) and tauro–α- and tauro–β-muricholic acid (Tα/βMCA) were decreased in both cecal contents and portal veins at both time points (figs. S2 to S5). Total cecal and portal venous BA concentrations were similar between the two groups at these early time points (figs. S2 to S5). In addition, levels of the conjugated BAs taurochenodeoxycholic acid (TCDCA), tauro-DCA (TDCA), and tauroursodeoxycholic acid (TUDCA) were decreased, and levels of the unconjugated BAs cholic acid (CA), chenodeoxycholic acid (CDCA), α-muricholic acid (αMCA), and βMCA were increased in portal veins at the 1-week time point (fig. S5). These findings indicate that changes in cecal and portal venous BA composition are associated with the onset of increased intestinal permeability in CDAHFD-fed rats and suggest that these metabolites could play a causal role in the development of gut barrier damage.

Intestinal permeability and inflammation are regulated in part by the BA-sensing farnesoid X receptor (FXR), which has been linked to NAFLD/NASH pathogenesis (*36*, *37*). In addition, FXR signaling modulates a tight negative feedback loop that controls BA synthesis in the liver (*38*). At 48 hours after dietary intervention, ileal *Fgf15* expression was similar in both groups when multiple lines of evidence for increased intestinal permeability were already observed in CDAHFD-fed animals (fig. S6A). The expression of BA synthesis and conjugation enzymes was not significantly affected in CDAHFD-fed rats at 48 hours of diet (fig. S6B). mRNA and protein levels of BA transporters were also unaffected in CDAHFD-fed rats compared to controls (fig. S6, C and D). Likewise, mRNA and protein levels of TGR5, a G protein–coupled receptor that has been previously implicated in the development of intestinal permeability, were not significantly different in CDAHFD-fed rats compared to HFD-fed animals (fig. S6, E and F). We found that cecal BSH activity in CDAHFD rats was significantly increased at 48 hours compared to control rats (fig. S6G) (*27*). These data raise the possibility that the decrease in conjugated BAs in CDAHFD-fed rats was driven, at least in part, by an increase in BA deconjugation by gut microbes. Together, our findings suggest that signaling-independent mechanisms are responsible for the earliest events that establish intestinal

barrier dysfunction in this animal model of pathogenic intestinal permeability.

In vivo BA compositions reflect increased intestinal permeability as disease progresses

UPLC-MS analysis revealed significant decreases in cecal unconjugated BAs in CDAHFD-fed rats at 6 weeks (e.g., αMCA, LCA, DCA, and UDCA) and in unconjugated, conjugated, and total BAs at 12 weeks (e.g., CA, αMCA, βMCA, LCA, DCA, UDCA, TDCA, tauro–omega-MCA, and TUDCA) compared to control animals (figs. S7 and S8). At the same time points, portal venous BA profiling revealed the inverse finding, with significantly higher concentrations of total and unconjugated BAs (e.g., CA, CDCA, αMCA, and βMCA) in CDAHFD-fed rats compared to controls (figs. S9 and S10). No significant differences were observed in the expression of genes involved in BA synthesis (*Cyp7a1*, *Cyp8b1*, and *Cyp27a1*) or transport (*Asbt* and *Osta/Ostb*) (fig. S11, A and B), indicating that the observed changes are unlikely to be the result of decreased BA synthesis or increased BA transport. These findings are consistent with the observation that CDAHFD-treated rats exhibit epithelial barrier damage and suggest that as disease progresses, increased intestinal permeability results in leakage of intestinal BAs into portal circulation.

Conjugated BAs protect intestinal epithelial monolayers from unconjugated BA-mediated damage in vitro

On the basis of our in vivo observations, we hypothesized that groups of conjugated or unconjugated BAs could be causally contributing to epithelial layer damage. To test this hypothesis, we used Caco-2 cells in transwell inserts as an in vitro model system. Once differentiated, these cells form a polarized monolayer that mimics the intestinal epithelium, and this system has been previously used to study the effect of metabolites on gut layer integrity (*39*). Gut permeability was assayed by measuring FITC-dextran (4 kDa) permeability through the monolayer and quantifying fluorescence in the basolateral chamber (*40*). We found that cecal extracts isolated from CDAHFD-fed rats at 48 hours and 1 week induced increased permeability compared to cecal extracts from control rats (Fig. 2A). These findings demonstrate that intestinal contents from CDAHFD-fed rats induce epithelial barrier permeability at early time points.

To test whether cecal BAs specifically induce epithelial permeability, we generated reconstituted pools of BAs that mimic the average physiological concentrations observed in rat ceca and tested their ability to induce permeability in Caco-2 monolayers in vitro. The 48-hour and 1-week CDAHFD BA pool induced significantly higher permeability than the HFD control BA pool (Fig. 2B). While the unconjugated BA pool alone induced a significant increase in permeability, the conjugated BA pool did not damage the monolayer barrier integrity (Fig. 2C). At later time points (1, 6, and 12 weeks), the addition of conjugated BAs to unconjugated BAs mitigated the severity of epithelial permeability compared to unconjugated BAs alone (Fig. 2C).

We next hypothesized that cecal conjugated BAs protect against the disruption of the epithelial integrity. To test this hypothesis, we generated equimolar pools of the predominant cecal BAs that we detected in vivo. We treated differentiated Caco-2 monolayers with increasing concentrations of (i) unconjugated BAs (βMCA, CA, DCA, UDCA, and CDCA), (ii) conjugated BAs (TβMCA, TCA, TDCA, TUDCA, and TCDCA), or (iii) combined BA pools followed by the permeability assessment (Fig. 2D).

At physiological concentrations of BAs in CDAHFD-fed rat cecal contents (~1000 to 4000 μM), the epithelial monolayer integrity was compromised after addition of unconjugated BAs, but damage was prevented by the addition of an equimolar concentration of conjugated BAs (Fig. 2E and figs. S2, S3, S7, and S8). Conjugated BAs alone did not disrupt the monolayer integrity at any concentrations tested. Similarly, while unconjugated BAs were toxic to cells, the equimolar addition of conjugated BAs abrogated this effect (Fig. 2F). Visualization of Caco-2 monolayers by hematoxylin and eosin (H&E) staining further confirmed that the toxic effects of unconjugated BAs were largely rescued by addition of conjugated BAs (Fig. 2G). Last, to assess the integrity of tight junctions in the epithelial monolayers, we performed transmission electron microscopy (TEM) on Caco-2 epithelial monolayers exposed to the above BA groups. We identified dilatations in the tight junctions of Caco-2 cells exposed to unconjugated BAs alone but not present in cells exposed to conjugated BAs alone or to a combination of both (Fig. 2H and fig. S12). These tight junction dilatations have been observed in ileal enterocytes of patients with Crohn's disease and correlate with increased permeability (*41*).

Epidermal growth factor receptor (EGFR) activation by unconjugated BAs such as CDCA and DCA has previously been shown to result in increased intestinal permeability (*19*). We did not observe differences in the EGFR activation in Caco-2 cells exposed to either control or CDAHFD BA pools (fig. S13). Together, these results demonstrate that while unconjugated BAs damage epithelial layers, conjugated BAs protect against intestinal epithelial damage and permeability in vitro through a mechanism that is independent of EGFR signaling.

Conjugated BAs sequester unconjugated BAs through the formation of micelles

We next sought to determine the signaling-independent mechanism by which conjugated BAs protect intestinal epithelial monolayers from unconjugated BA-mediated permeability in vitro. BAs are detergents and effectively solubilize fats and vitamins by forming micelles in the intestine (*42*). We hypothesized that when combined, conjugated BAs form micelles with unconjugated BAs, sequestering unconjugated BAs away from the epithelial cells. To test this hypothesis, we assessed the critical micelle concentration (CMC) of these BA populations using a fluorescent probe (*43*). The CMC is the minimum concentration of a surfactant above which micelle formation takes place and is influenced by the physical properties of the surfactant and environmental conditions. Unconjugated BAs are expected to have a higher CMC compared to conjugated BAs (*44*). If micelles were formed after combining unconjugated and conjugated BA populations, then we would expect the CMC of the combined populations to be lower than that seen with unconjugated BAs alone. Consistent with this hypothesis, the combined pool CMC was 4.2 mM, while the unconjugated and conjugated BA pool CMCs were 6.7 and 4.0 mM, respectively (Fig. 3A). The addition of 80 mM urea prevented micelle formation as previously described (Fig. 3A) (*42*). We also performed direct visualization of micelles using negative staining electron microscopy (EM). At 5 mM concentration, no micelles were visualized in the unconjugated BA pool, while micelles were seen in the conjugated BA pool, consistent with our CMC determinations and total cecal BA quantification in CDAHFD-fed rats at the 48-hour time point (Fig. 3B and fig. S2). Combining BA pools resulted in larger micelles, while urea prevented micelle

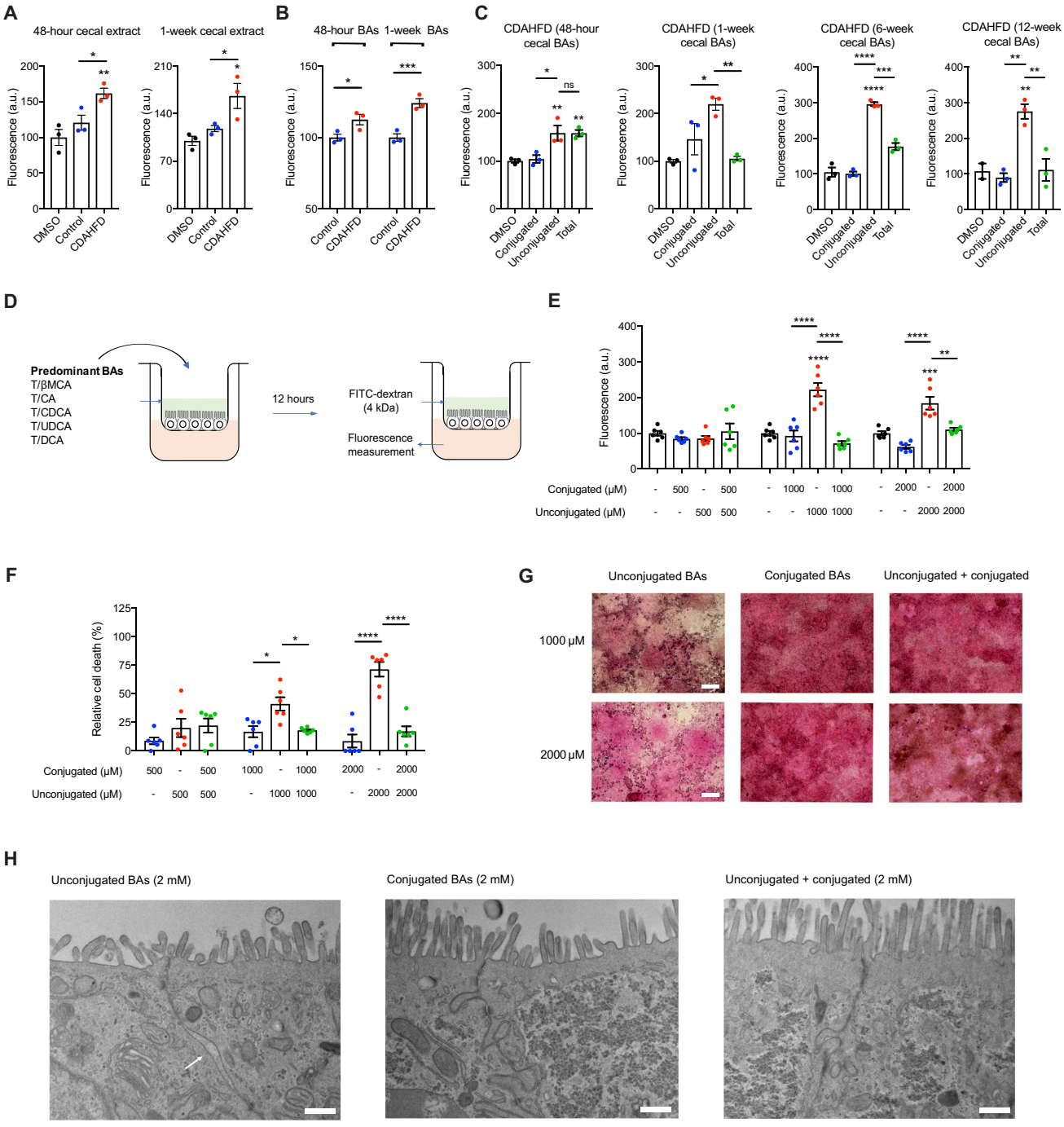

Fig. 2. Conjugated BAs protect epithelial monolayers from unconjugated BA-induced permeability. (**A**) Cecal extracts from CDAHFD-fed rats at early time points caused increased epithelial permeability. Caco-2 monolayer permeability measured by FITC-dextran passage into the basolateral chamber after exposure to indicated purified cecal extracts over 12 hours. DMSO, dimethyl sulfoxide. (**B**) Forty-eight–hour and 1-week CDAHFD BA pool induced significantly higher permeability than the HFD BA pool. (**C**) Conjugated BAs alone did not increase Caco-2 monolayer permeability at concentrations found in the cecum of CDAHFD rats, and when combined with unconjugated BAs, conjugated BAs are protected against unconjugated BA-induced permeability. (**D**) Schematic of in vitro permeability experiment. (**E**) Conjugated BAs protected against unconjugated BA-induced Caco-2 monolayer permeability at physiologic concentrations ($n = 6$ per group). (**F**) Conjugated BAs protected epithelial monolayers from unconjugated BA-induced cell death. Cell viability of Caco-2 cells measured by MTT assay ($n = 6$ per group). (**G**) Conjugated BAs protected the physical integrity of epithelial monolayers from unconjugated BA-induced damage. Representative light microscopy images of hematoxylin and eosin (H&E)–stained Caco-2 monolayers after exposure to BA pools. Scale bars, 20 μm. (**H**) Conjugated BAs prevented the development of unconjugated BA-induced tight junction dilatation. Representative transmission electron microscopy (TEM) images of Caco-2 cells from transwells after exposure to BA pools at indicated concentrations. The white arrow points to tight junction dilatation. Scale bars, 500 nm. See the Supplementary Materials for additional representative TEM images. Unless otherwise specified, all experiments were performed in biological triplicate. See Materials and Methods for statistical analyses. *$P < 0.05$, **$P < 0.005$, ***$P < 0.001$, and ****$P < 0.0001$. Bars represent means ± SEM.

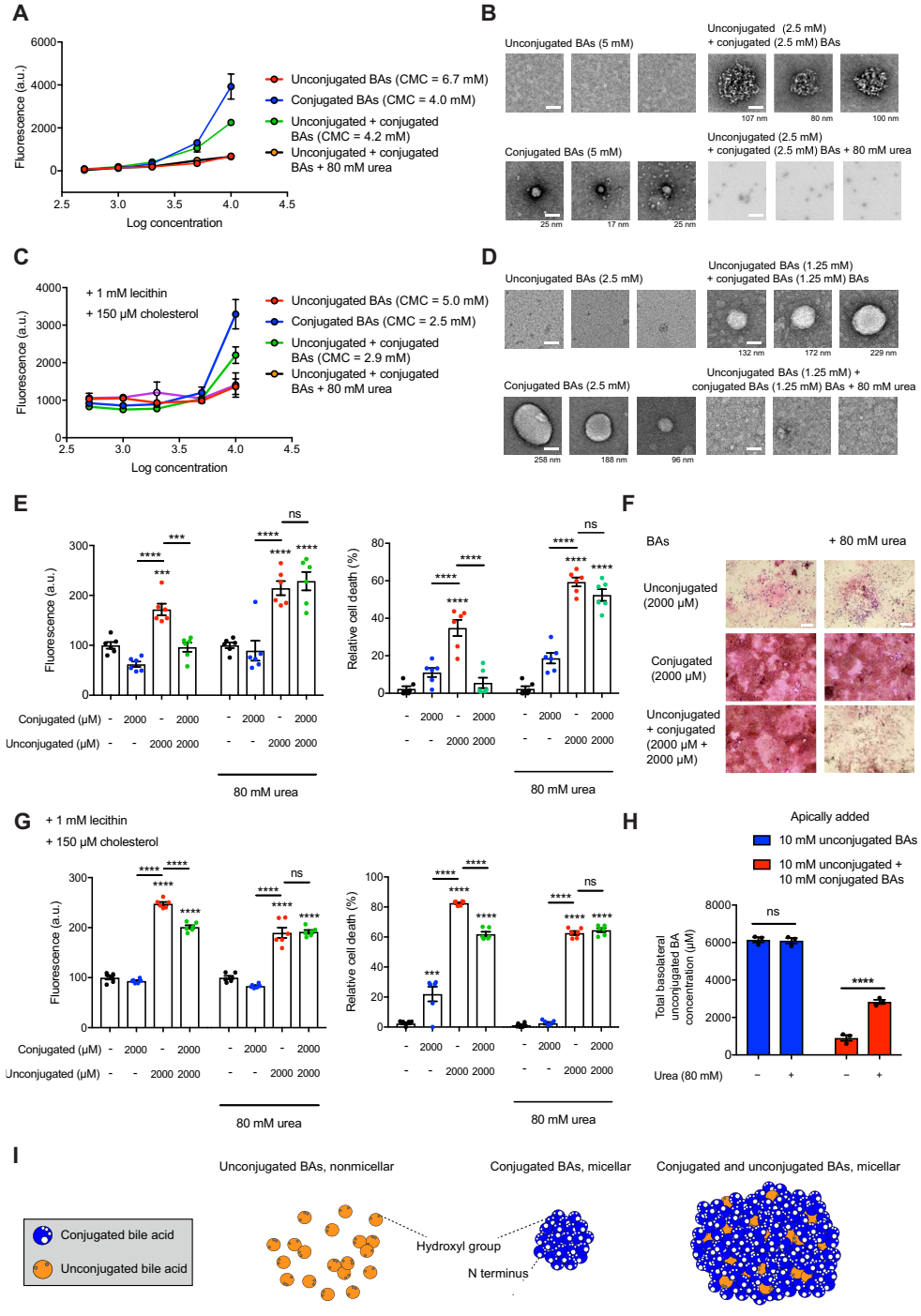

Fig. 3. Conjugated and unconjugated BAs form micelles that sequester unconjugated BAs and prevent epithelial damage. (**A**) Conjugated and combined BAs exhibited lower CMCs than unconjugated BAs alone. Micelle formation was disrupted after addition of urea (80 mM). (**B**) EM images of micelles formed from BAs at indicated concentrations with or without urea. Scale bars, 50 nm (diameter of micelle indicated beneath each image). (**C**) Conjugated and combined BAs exhibited lower CMCs than unconjugated BAs alone in the presence of lecithin and cholesterol. (**D**) EM images of micelles formed from BAs at indicated concentrations with lecithin and cholesterol. Scale bars, 50 nm (diameter of micelle indicated beneath each image). (**E**) Micelle formation was necessary for the protective effect of conjugated BAs on epithelial permeability and viability. Permeability measured by fluorescence (FITC-dextran) in basolateral chamber and Caco-2 viability measured by MTT assay with or without urea ($n = 6$ per group). (**F**) Micelle formation was necessary for the protective effect of conjugated BAs on epithelial layer integrity. Representative light microscopy images of H&E-stained Caco-2 monolayers in transwells with or without urea. (**G**) Micelle formation was necessary for the protective effect of conjugated BAs on epithelial permeability and viability in the presence of lecithin and cholesterol ($n = 6$ per group). (**H**) Addition of urea to mixed BAs led to increased unconjugated BA passage across Caco-2 monolayers. Quantification of basolateral concentrations of unconjugated BAs by UPLC-MS. (**I**) Model for sequestration of unconjugated BAs in micelles by conjugated BAs. BAs shown in cross section and micellar shape depictions based on previous micelle models (*64*, *65*). Unless otherwise specified, all experiments were performed in biological triplicate. See Materials and Methods for statistical analyses. ***$P < 0.001$ and ****$P < 0.0001$. Bars represent means ± SEM.

formation entirely. Thus, in the presence of physiological concentrations of conjugated BAs, unconjugated BAs are sequestered in micelles.

The intestinal lumen is a complex environment that contains fats, cholesterol, and other dietary and host-derived molecules in addition to BAs. Biliary phospholipids such as lecithin lower CMCs for BA-mixed micelle formation, while cholesterol raises CMCs (*45*, *46*). Therefore, we investigated whether conjugated BAs sequester unconjugated BAs in micelles in the presence of physiological levels of phospholipids and cholesterol (fig. S14A) (*47*, *48*). Consistent with previous studies, we found that the CMCs of BA groups shift in the presence of lecithin and cholesterol (Fig. 3C). Similar to our results with BAs alone, the CMC of the combined pool (2.5 mM) was similar to the CMC of the conjugated pool (2.5 mM), and both CMCs were lower than the unconjugated BA pool CMC (5 mM) (Fig. 3C). The addition of 80 mM urea prevented mixed micelle formation as previously described (Fig. 3, A to C) (*42*). Visualization of micelles using negative staining EM confirmed the CMCs for BA groups in the presence of cholesterol and lecithin (Fig. 3D). Together, these results suggest that in the presence of physiological concentrations of intestinal components such as lecithin and cholesterol, conjugated BAs sequester unconjugated BAs in micelles.

To investigate whether the protective effects of conjugated BAs are micelle dependent, we tested whether BA pools with or without lecithin and cholesterol induce intestinal permeability in the presence of 80 mM urea, a concentration that prevents micelle formation (Fig. 3, A to D) without inducing cell death in Caco-2 cells (fig. S14B). Notably, conjugated BAs protected against epithelial damage in the presence of lecithin and cholesterol, and the addition of urea resulted in loss of conjugated BA-mediated protection of epithelial barrier integrity and cell viability under all conditions tested (Fig. 3, E to G). We also exposed Caco-2 monolayers to combined BA pools in the presence or absence of urea and quantified the amount of unconjugated BAs that passed through the monolayer into the basolateral chamber by UPLC-MS. We observed significantly increased amounts of unconjugated BAs in the basolateral chamber in the presence of urea, providing further evidence that micelle formation prevents epithelial damage and permeability (Fig. 3H).

Together, our data provide evidence that unconjugated BAs lead to increased permeability across an intestinal epithelial monolayer by inducing cell death. Further, these effects are prevented by the addition of conjugated BAs, which form BA micelles with unconjugated BAs in vitro (Fig. 3I). These data demonstrate that conjugated BAs protect against gut barrier dysfunction through their physicochemical properties.

BSH inhibition by AAA-10 prevents altered intestinal permeability and hepatic inflammation in CDAHFD-fed rats

Because conjugated BAs appear to protect against intestinal epithelial damage, we hypothesized that a decrease in microbial BA deconjugation by BSH might attenuate intestinal permeability in CDAHFD-fed rats. We recently reported the development of a covalent, gut-restricted, small-molecule inhibitor of gut bacterial BSHs, AAA-10, a compound that effectively inhibits BSH activity and increases the abundance of conjugated BAs in vivo (Fig. 4A) (*26*). We thus hypothesized that treatment of CDAHFD-fed rats with AAA-10 would prevent increased intestinal permeability. A dose of AAA-10 or vehicle control (10 mg/kg) was administered via gavage twice a day for 7 days to CDAHFD-fed rats (Fig. 4B). AAA-10 administration led to ~20 to 30 μM AAA-10 in cecal contents 48 hours and 1 week after gavage (Fig. 4C). No AAA-10 was detected in peripheral blood (fig. S15A), a finding that is consistent with our previous results (*26*) and indicates that this BSH inhibitor exhibits low systemic exposure. We found that AAA-10 reduced cecal BSH activity of CDAHFD-fed rats (Fig. 4D) and significantly increased both the abundance of conjugated BAs as a group (Fig. 4E) and the concentrations of individual conjugated BAs by 1 week without affecting animal weights (figs. S15B and S16). Notably, we observed significant decreases in levels of portal venous LPS, suggestive of increased intestinal barrier function in AAA-10–treated rats compared to vehicle-treated animals (Fig. 4F). Furthermore, we observed normalization of ZO-1 localization and expression, suggesting that AAA-10 treatment prevented the development of intestinal permeability in CDAHFD-fed rats (Fig. 4G).

As intestinal permeability has been linked to translocation of intestinal products that further exacerbate hepatic inflammation (*4*), we evaluated the impact of 8-day AAA-10 treatment on liver phenotypes (Fig. 5A). Consistent with our previous results, we found that the BA pool shifted toward conjugated BAs in AAA-10–treated compared to control-treated rats (fig. S17). Mild weight loss was observed in the AAA-10–treated animals (fig. S18A), consistent with our previous report that genetic removal of bacterial BSH causes altered metabolic phenotypes including reduced weight gain on an HFD (*49*). We did not observe significant weight loss in AAA-10–treated rats in the 7-day experiment (fig. S15B), and we observed similar changes in ZO-1 localization and expression in both experiments (Fig. 4G and fig. S18B), suggesting that AAA-10–mediated protection against intestinal permeability occurred independent of weight loss. Colonic TGR5 expression was not affected by AAA-10 treatment, consistent with our prior data that AAA-10 does not agonize TGR5 in Caco-2 cells (fig. S18C). We also assessed the effect of AAA-10 or vehicle treatment on normal chow-fed rats and found no significant differences between the groups in liver or kidney function, body weight, or caloric intake (fig. S19), suggesting that AAA-10 itself was nontoxic and that differences between groups are directly related to changes in intestinal BA composition.

We observed substantial histologic improvements in AAA-10–treated rats compared to vehicle-treated controls. Specifically, AAA-10–treated rats exhibited significantly less hepatic steatosis, lobular inflammation, and hepatocyte ballooning (Fig. 5, B and C). Consistent with these results, we observed significant decreases in serum measures of hepatic inflammation including alanine aminotransferase (ALT), aspartate aminotransferase (AST), and alkaline phosphatase (ALP) in AAA-10–treated animals (Fig. 5D). Last, we observed decreased expression of proinflammatory and profibrotic genes in treated rats (Fig. 5, E and F). Together, our findings demonstrate that treatment with the gut-restricted BSH inhibitor AAA-10 prevents the development of intestinal barrier dysfunction and liver damage in CDAHFD-fed rats.

Glyco-conjugated BAs form protective micelles in vitro

While rodents have only tauro-conjugated BAs, humans have a mixture of glyco- and tauro-conjugated BAs, with the former dominating the pool in a ratio of 3:1 (Fig. 6A) (*14*). Further, microbial BSHs in the human intestine hydrolyze glyco-conjugated BAs to their unconjugated forms (*14*). To test whether glyco-conjugated BAs are also capable of forming micelles to sequester damaging unconjugated BAs, we determined CMCs of these BA populations as described

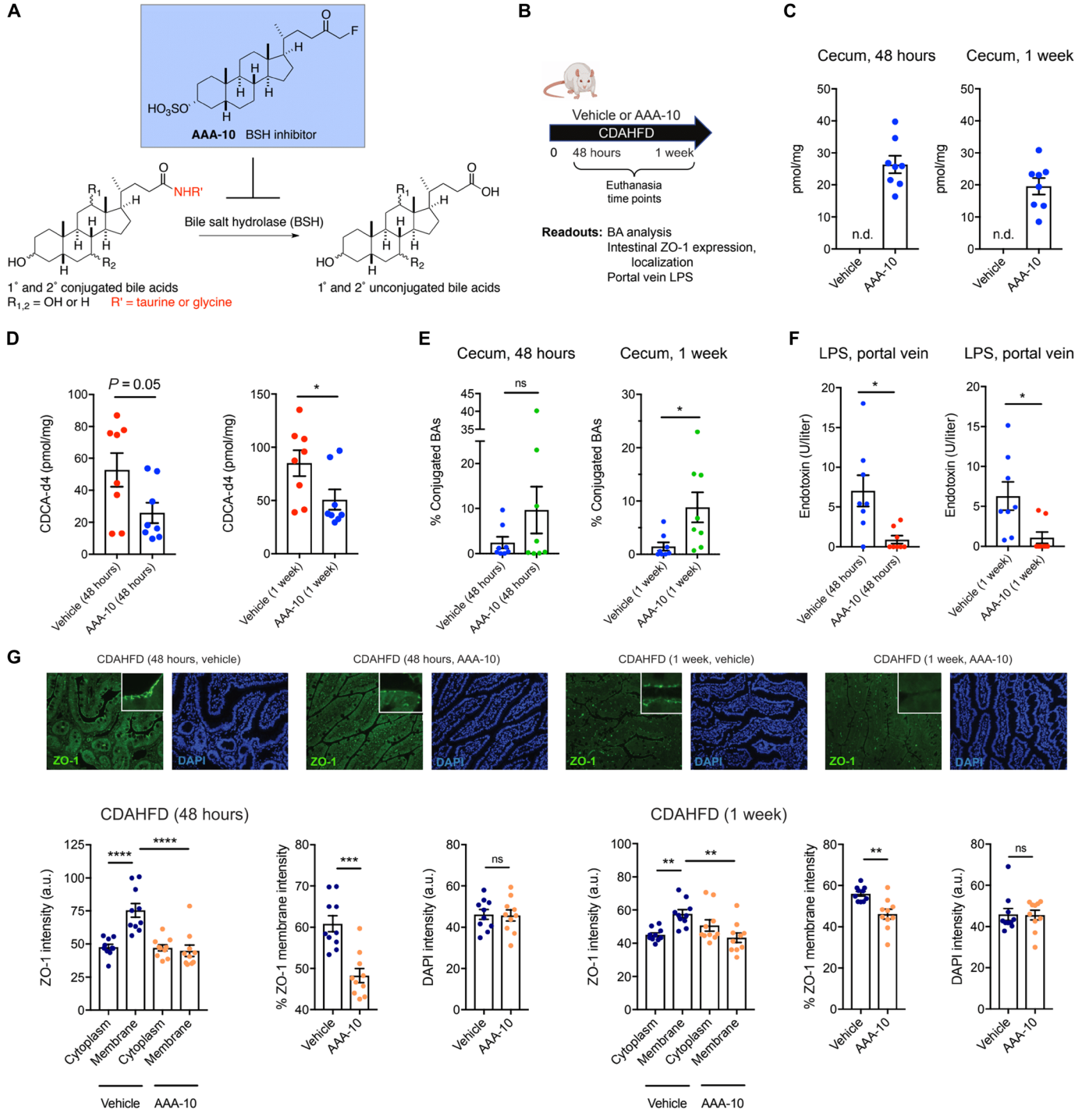

Fig. 4. BSH inhibition increases intestinal conjugated BAs and prevents intestinal barrier dysfunction in CDAHFD-fed rats. (**A**) Schematic for the inhibition of bacterial BSH activity by the covalent pan-BSH inhibitor AAA-10 (*26*, *27*). (**B**) Schematic of rat intestinal permeability prevention experiment. Rats were fed CDAHFD and administered either AAA-10 (10 mg/kg per dose) or vehicle twice daily by gavage. Rats were euthanized at 48 hours or 1 week. Tissues and blood were collected for metabolite quantification and evaluation of intestinal injury markers ($n = 8$ per for all time points). (**C**) UPLC-MS analysis of cecal contents of vehicle- and AAA-10–treated animals. Cecal AAA-10 levels that were within the concentration range were previously shown to be effective for inhibiting BSH activity (*26*, *27*). n.d., not detected. (**D**) Cecal BSH activity was reduced after 1 week of AAA-10 treatment. BSH activity was determined by quantifying conversion of GCDCA-d4 to CDCA-d4 in feces from vehicle- or AAA-10–treated animals (two-tailed Welch's *t* test). (**E**) Cecal conjugated BA abundance was significantly increased in AAA-10–treated rats after 1 week (two-tailed Welch's *t* test; see the Supplementary Materials for concentrations of total and individual BAs in cecal contents at 1 week). (**F**) Portal venous LPS levels were reduced in AAA-10–treated rats after 48 hours and 1 week of AAA-10 treatment (two-tailed Welch's *t* test). (**G**) AAA-10 treatment prevented aberrant ZO-1 subcellular localization. ZO-1 immunofluorescence and DAPI counterstaining of rat ileum from vehicle- and AAA-10–treated CDAHFD-fed rats at 48 hours and 1 week ($n = 10$ intestinal cells quantified per group; see Materials and Methods for statistical analyses). $^*P < 0.05$, $^{**}P < 0.005$, $^{***}P < 0.005$, and $^{****}P < 0.0001$. Bars represent means ± SEM.

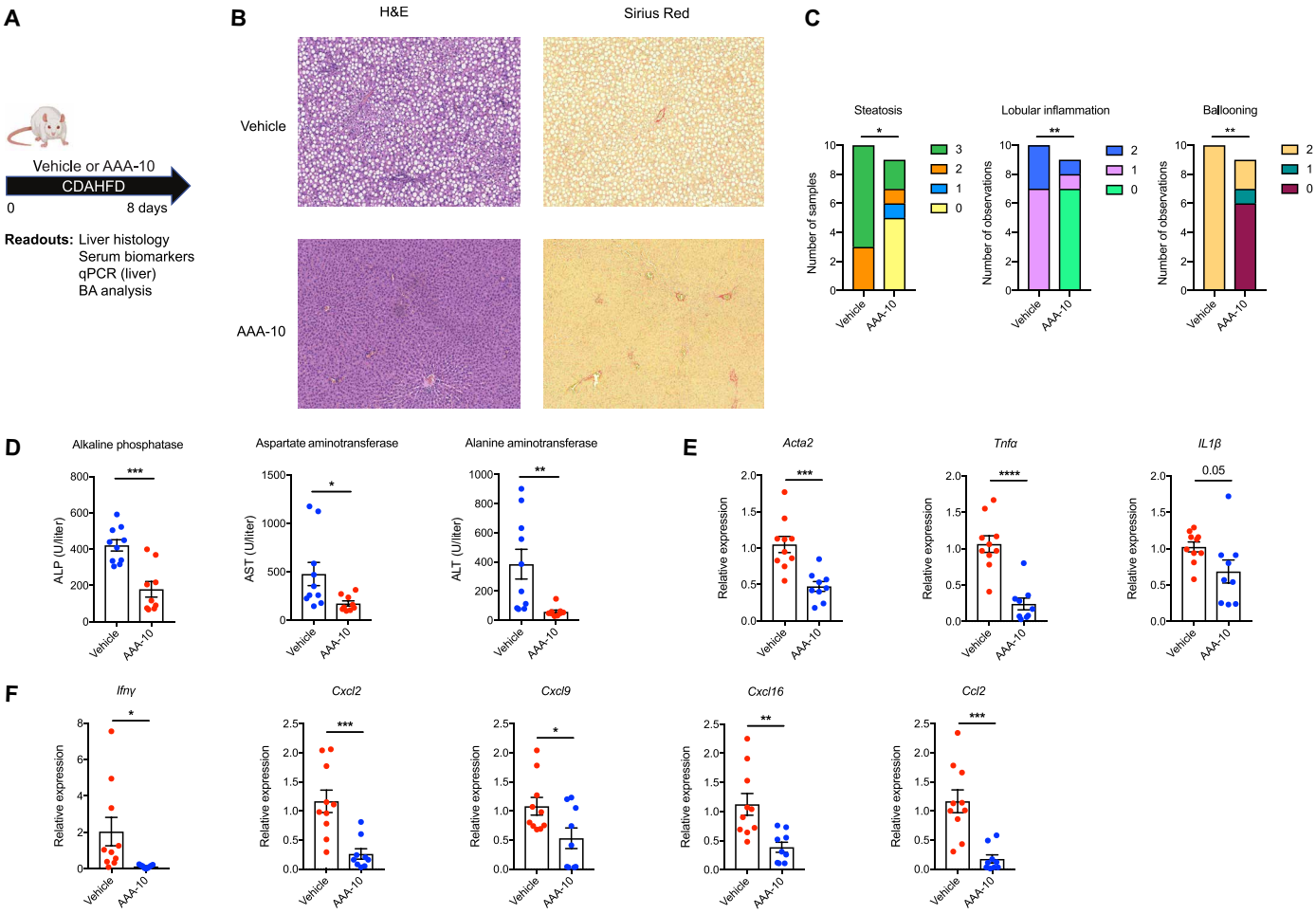

Fig. 5. BSH inhibition prevents hepatic inflammation in CDAHFD-fed rats. (**A**) Schematic of rat liver damage prevention experiment. Rats were fed CDAHFD and administered either AAA-10 (10 mg/kg per dose) or vehicle twice daily by gavage. Rats were euthanized after 8 days. Liver tissue and blood were collected for metabolite quantification and evaluation of liver injury markers ($n = 10$ in vehicle group and $n = 9$ in AAA-10 group for all time points). (**B**) AAA-10 treatment prevented development of hepatic steatosis and inflammation in CDAHFD-fed rats. Representative H&E staining of liver tissue is shown. (**C**) AAA-10 treatment prevented development of hepatic inflammation. Histologic scoring of steatosis, hepatocyte ballooning, and lobular inflammation in vehicle- and AAA-10–treated animals. Mann-Whitney test. (**D**) Serum alanine aminotransferase (ALT), aspartate aminotransferase (AST), and alkaline phosphatase (ALP) levels were decreased in AAA-10–treated compared to vehicle-treated rats (two-tailed Welch's *t* tes)t. (**E** and **F**) AAA-10 treatment attenuated hepatic gene expression of proinflammatory and profibrotic genes in CDAHFD-fed rats as determined by reverse transcription qPCR (RT-qPCR) analysis of indicated genes (two-tailed Welch's *t* test). $^*P < 0.05$, $^{**}P < 0.005$, $^{***}P < 0.0005$, and $^{****}P < 0.0001$. Bars represent means ± SEM.

above (Fig. 3, A to D). We used an equimolar mix of (i) glyco-conjugated BAs [glyco-cholic acid (GCA), glyco-deoxycholic acid (GDCA), glyco-ursodeoxycholic acid (GUDCA), and glyco-chenodeoxycholic acid (GCDCA)] or (ii) combined BA pools containing the same unconjugated BAs as used above (βMCA, CA, DCA, UDCA, and CDCA). Glyco-conjugated BAs exhibited a lower CMC than tauro-conjugated BAs (3.64 compared to 4.0 mM, respectively) (Figs. 6B and 3A). Consistent with this observation and our previous results, the CMC of the combined pool with glyco-conjugated BAs was 3.60 mM, while the CMC of the combined pool of tauro-conjugated BAs was 4.2 mM (Fig. 6B and 3A). We also performed direct visualization of micelles using negative staining EM. At 5 mM concentration, no micelles were visible in the unconjugated BA pool, while micelles were observed in the glyco-conjugated and combined BA pools, consistent with our CMC determinations (Fig. 6C). In the presence of physiological levels of lecithin and cholesterol as described above (Fig. 3, C and D), the CMCs of BA groups were reduced, but the phenomenon that the combined BA pool and the glyco-BA pool harbored lower CMCs than the unconjugated pool was maintained (CMCs = 1.0, 2.3, and 5.0 mM for combined BAs, glyco-conjugated BAs, and unconjugated BAs, respectively; Fig. 6, D and E). Together, these results suggest that glyco-conjugated BAs form micelles with unconjugated BA species with equal to or greater efficiency than tauro-conjugated BAs.

Next, we sought to determine whether glyco-conjugated BAs would also protect the intestinal epithelium from the damaging effects of unconjugated BAs. Using transwell-differentiated Caco-2 cells, we found that unconjugated BA-induced epithelial monolayer damage was prevented by addition of an equimolar concentration of glyco-conjugated BAs (Fig. 6F). Glyco-conjugated BAs alone did not disrupt monolayer integrity at any concentrations tested. Similarly, while unconjugated BAs were toxic to cells, the equimolar

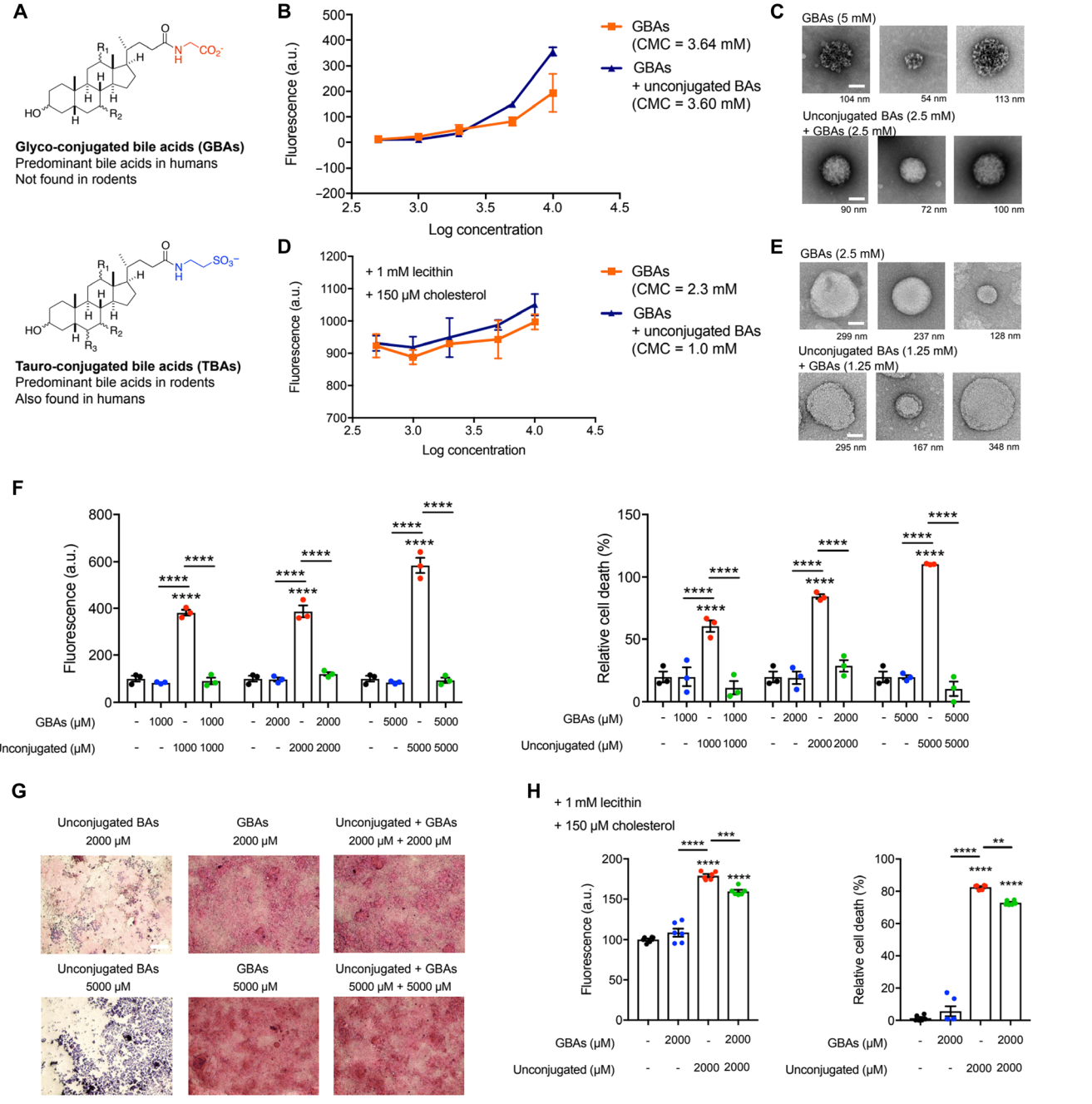

Fig. 6. Predominant human glyco-conjugated BAs sequester unconjugated BAs in micelles and prevent epithelial damage in vitro. (**A**) Structures of glyco- and tauro-conjugated BAs (GBAs and TBAs, respectively). (**B**) Pools of glyco-conjugated BAs alone and glyco-conjugated BAs plus unconjugated BAs exhibited CMCs of 3.64 and 3.60 mM, respectively, indicating efficient micelle formation. (**C**) EM images of micelles formed from BA pools at indicated concentrations. Similar to tauro-conjugated BAs, while detectable micelles were visible in the glyco-conjugated BAs alone or unconjugated BAs plus glyco-conjugated BA pools, no detectable micelles were visible in the unconjugated BAs pool. Scale bars, 50 nm (diameter of micelle indicated beneath each image). (**D**) CMCs of pools of glyco-conjugated BAs alone and glyco-conjugated BAs plus unconjugated BAs in the presence of lecithin and cholesterol. (**E**) EM images of micelles formed from BA pools at indicated concentrations in the presence of lecithin and cholesterol. Scale bars, 50 nm (diameter of micelle indicated beneath each image). (**F**) Glyco-conjugated BAs protected against unconjugated BA-induced Caco-2 monolayer permeability at physiologic concentrations. Glyco-conjugated BAs protected epithelial monolayers from unconjugated BA-induced cell death. Cell viability of Caco-2 cells measured by MTT assay. (**G**) Glyco-conjugated BAs protected the physical integrity of epithelial monolayers from unconjugated BA-induced damage. Representative light microscopy images of H&E-stained Caco-2 monolayers after exposure to BA pools. Scale bar, 20 μm. (**H**) Glyco-conjugated BAs protected against unconjugated BA-induced Caco-2 monolayer permeability and cell death at physiologic concentrations in the presence of lecithin and cholesterol ($n = 6$ per group). Unless otherwise specified, all experiments were performed in biological triplicate. See Materials and Methods for statistical analyses. $^{**}P < 0.005$, $^{***}P < 0.0005$, and $^{****}P < 0.0001$. Bars represent means ± SEM.

addition of glyco-conjugated BAs abrogated this effect (Fig. 6F). Visualization of Caco-2 monolayers by H&E staining further confirmed that the toxic effects of unconjugated BAs were largely prevented by addition of glyco-conjugated BAs (Fig. 6G). Last, in the presence of lecithin and cholesterol, glyco-conjugated BAs protected the monolayers from unconjugated BA-mediated permeability and cell death, although the degree of protection was lessened compared to the conditions of BAs alone (Fig. 6H). Together, these results suggest that the predominant human-derived glyco-conjugated BAs are also capable of sequestering unconjugated BAs in micelles and protecting against epithelial permeability.

DISCUSSION

In this study, we show that the onset of small intestine permeability is associated with decreased intestinal and portal conjugated BA abundance in a diet-induced animal model of intestinal barrier and liver damage. Furthermore, we demonstrate a signaling-independent mechanism by which conjugated BAs protect intestinal epithelial barriers from damage in vitro via the sequestration of unconjugated BAs in micelles. We then demonstrate that inhibition of gut bacterial BSH activity increases the abundance of cecal conjugated BAs and prevents the development of small intestinal barrier dysfunction and liver inflammation in vivo. Last, we show that both tauro-conjugated BAs and glyco-conjugated BAs protect against unconjugated BA-induced epithelial barrier damage in vitro. Because glyco- and tauro-conjugated BAs are the two conjugated BA forms found in humans, our data suggest that conjugated BAs could be protective in the human gut.

The CDAHFD-fed rat model we used here to investigate pathogenic intestinal permeability is a rodent model of chronic liver disease, including NAFLD and NASH progression (*25*). Gut dysbiosis is a central feature of human NAFLD/NASH and has been proposed to contribute to the development of these conditions (*50*, *51*). Likewise, changes in serum BA profiles have been reported to correlate with disease severity in patients with NAFLD/NASH (*52*–*54*). However, causal connections between gut bacteria, BA metabolism, and NAFLD/NASH in humans have not yet been established. Our data raise the possibility that bacterial BA deconjugation may be causally contributing to NAFLD/NASH progression. We observed higher levels of BSH activity in CDAHFD-treated rats compared to control animals. Future analyses will help uncover whether correlations exist between fecal BA levels, BSH activity, and disease severity in human patients. In addition, further studies in different animal models of pathogenic intestinal permeability will reveal whether pharmacological BSH inhibition can prevent or ameliorate gut barrier damage. Nonetheless, the finding that BSH inhibition prevents intestinal permeability and liver damage in CDAHFD-fed rodents, a diet-induced model of liver cirrhosis, suggests that modulating the in vivo BA pool by selective targeting of the gut microbiota could be investigated as a treatment path for diseases characterized by intestinal barrier disruption.

Intestinal barrier function has been implicated in the pathogenesis of a variety of diseases. However, the molecular mechanisms that trigger or protect against intestinal permeability defects are incompletely defined (*23*). While individual BAs have been identified as key signaling molecules, our work demonstrates that, as a result of their role as detergents, micellar BAs are important for the maintenance of intestinal barrier integrity. It has been shown that hydrophilic BAs, including conjugated BAs, protect against cytotoxicity induced by hydrophobic BAs, including many unconjugated species (*55*–*57*). However, before our work, the connection between the efficiency of micelle formation by conjugated BAs and their ability to protect against unconjugated BA-induced epithelial barrier damage had not been established. Here, we demonstrate that conjugated BAs form micelles with unconjugated BAs at physiologically relevant concentrations in vitro. Micelle formation leads to sequestration of hydrophobic, unconjugated BAs away from epithelial cells and prevents cell death and tight junction dysfunction. These data demonstrate that distinct classes of BAs elicit differential effects on intestinal epithelial permeability and delineate a mechanism by which one of these classes, conjugated BAs, protects against epithelial damage in vitro.

Cholesterol, phospholipids, and lipid hydrolysis products form mixed micelles with BAs in bile and in the intestine (*58*). We have demonstrated that, even in the presence of lecithin and cholesterol, conjugated BAs protect against epithelial damage. Although we used physiologically relevant concentrations of lecithin and cholesterol, we only tested one concentration of these compounds, and their levels are likely to vary both over time and between individuals in vivo. Moreover, the gut contains a complex mixture of host- and diet-derived metabolites and conditions that cannot be fully recapitulated in an in vitro setting. Furthermore, it is not yet known whether the micellar protection mechanism is operable in vivo. To our knowledge, there are currently no selective means of preventing micelle formation in vivo. Nonetheless, by inhibiting BSH activity using AAA-10, we selectively shifted the in vivo BA pool toward conjugated BAs. These experiments suggest that, consistent with our in vitro data, conjugated BAs protect against epithelial barrier damage in vivo.

The treatment of CDAHFD-fed rats with a gut-restricted BSH inhibitor not only prevented intestinal permeability but also protected against the development of hepatic inflammation and steatosis. The prevention of liver damage is likely multifactorial, and effects including the decreased translocation of bacterial products such as LPS and mild weight loss may contribute. The weight loss observed is likely a result of BSH-dependent metabolic changes as we have previously reported (*49*). Germ-free mice, which lack BSH and therefore have high levels of intestinal conjugated BAs, are resistant to development of hepatic steatosis (*59*). Moreover, colonization of germ-free mice on a HFD with BSH-containing bacteria induces hepatic steatosis, a phenotype that can be prevented by the deletion of BSH (*49*). Our results here demonstrate that shifting the in vivo BA pool to enrich for conjugated BAs can not only prevent pathogenic intestinal permeability but can also prevent fat deposition and inflammation in the host liver.

Overall, our findings link changes in the intestinal BA pool, specifically conjugated BAs, with maintenance of the intestinal epithelial barrier in vivo. Our study also reveals that bacterial BSH enzymes regulate metabolites that control gut barrier integrity, thereby providing a mechanistic link between the microbiome and the development of pathogenic intestinal permeability. Our findings suggest that strategies that reduce BSH activity in the human gut microbiome could be developed as a previously unexplored paradigms to treat intestinal barrier dysfunction.

MATERIALS AND METHODS

Animals

Eight-week-old Wistar rats were purchased from Charles River Laboratories (Wilmington, MA) and housed in a specific pathogen–free

environment (maximum of four per cage). After 10 days of acclimation, rats were initiated on either a control HFD (60 kcal% fat; Research Diets D12492) or CDAHFD (L-amino acid diet with 60 kcal% fat with 0.1% methionine without added choline; Research Diets A06071302) ad libitum for either 48 hours or 1 week (either 7 or 8 days). At the time of sacrifice, rats were anesthetized using ketamine (100 mg/kg) and xylazine (10 mg/kg) intraperitoneally followed by portal vein blood draw and terminal cardiac puncture.

In vivo intestinal permeability assay

Intestinal permeability was assessed by in vivo FITC-dextran (FD4; Sigma-Aldrich, St. Louis, MO) permeability assay as described previously (*60*). Rats were fasted for 4 hours and then had blood collected via tail vein puncture to assess background fluorescence. Rats were then gavaged with FITC-dextran (0.4 mg/g body weight) 4-kDa solution, and blood was collected by terminal cardiac puncture. Fluorescence intensity in the serum determined at 530 nm with excitation at 485 nm. Relative fluorescence units determined by subtracting the phosphate-buffered saline (PBS) blank fluorescence from all samples and then subtracting the pregavage fluorescence from the postgavage fluorescence. FITC-dextran concentrations were determined from a standard curve generated by serial dilutions of FITC-dextran.

AAA-10 treatment

After initiation of CDAHFD diet, rats were split into two groups and were gavaged twice a day with either AAA-10 (10 mg/kg) dissolved in 5% Captisol (Ligand, San Diego, CA) and 5% dimethyl sulfoxide (DMSO) in PBS or an equal volume of 5% Captisol and 5% DMSO in PBS.

RNA extraction and RT-qPCR

Total RNA was extracted from liver tissue using TRizol (Invitrogen) according to the manufacturer's instructions and subsequently treated with DNase I (Promega). cDNA was generated using the RevertAid First Strand cDNA Synthesis kit according to manufacturer's instructions (Thermo Fisher Scientific) and reverse transcription qPCR (RT-qPCR) was performed using the Power SYBR Green Master Mix Kit (Thermo Fisher Scientific). Expression of *GAPDH* was used to standardize the samples, and the results are expressed as a ratio relative to control. The genes for which expression was determined, and the primer sequences used in this study can be found in table S1.

Serum processing

A cardiac terminal blood withdrawal was performed at the time of sacrifice. Blood was allowed to clot for 2 hours at room temperature before centrifugation at 2000 rpm for 10 min at 4°C. Serum was isolated and stored at −80°C. Biochemical markers of liver injury were measured, including ALP, ALT, and AST (DRI-CHEM 4000 Analyzer, Heska).

Histology and immunofluorescence

Formalin-fixed paraffin-embedded liver and ileum tissues were sectioned at a thickness of 4 μm. Slides were stained with H&E at the MGH Cytopathology Core. Slides were stained with Sirius Red for fibrosis staging. Slides were blindly reviewed by a blinded pathologist to grade steatosis, inflammation, and fibrosis using criteria modeled on human NASH histologic scoring systems. Similarly, for intestine, slides were evaluated for intestinal inflammation, epithelial hyperplasia, and goblet cell loss. For immunofluorescence, sections were stained for ZO-1 (Abcam, Cambridge, MA) with detection by appropriate secondary antibodies labeled with Alexa Fluor 488 according to the manufacturer's instructions. Hydroxyproline was quantified by high-performance LC (HPLC) analysis as previously described (*61*).

For ZO-1 staining intensity measurement, images were processed and analyzed with Adobe Photoshop CC software. Matched images were taken with the same exposure and were processed and analyzed identically. The two-dimensional image intensities of ZO-1 fluorescence (in pixels) of $n = 10$ randomly selected cells in micrographs from each condition were measured using Photoshop software (Adobe) and plotted in GraphPad Prism.

LPS measurement assay

Bacterial endotoxin measurement in portal serum samples was performed using the Lonza Pyrogent Turbidometric LAL Assay Kit (Lonza, N383) according to manufacturer's instructions. Briefly, serial dilutions of prepared serum samples were made using the LAL reagent water provided in the kit, followed by incubation for 15 min at 37°C. Samples were then mixed with the reconstituted Pyrogent reagent from the kit, followed by kinetic turbidometric analyses in a SpectraMax M5 plate reader (Molecular Devices, San Jose, CA) at the Institute of Chemistry and Cell Biology (ICCB)–Longwood Screening Facility at Harvard Medical School (HMS). LPS amount in samples was deduced using standard curves generated from stock provided in the kit and linear regression calculation.

BA and cholesterol analysis

BA analyses were performed using a previously reported method (*49*). Cholesterol quantification was carried out by analysis of the extract via gas chromatography–mass spectrometry (GC-MS) (Agilent Technologies 7890B GC System coupled to a 5977B electron ionization mass spectrometry detector). Briefly, 1 μl of sample was injected into the inlet held at 320°C and 11.65 psi on a split stream at a 5:1 ratio. The sample was run on an Agilent J&W HP-5ms Ultra Inert column (model 19091S-433 UI) held at 120°C for 1 min, ramping to 308°C at 50°C/min, then increasing to 315°C over the following minute. The column was held at 315°C for 4 min before returning to 120°C. The detector was set to selected ion monitoring for mass/charge ratio of 386.

Reagents

Stock solutions of all BAs were prepared by dissolving compounds in molecular biology grade DMSO (VWR International). Cholesterol standard was prepared by dissolving in ethanol. These solutions were used to establish standard curves. HPLC grade solvents were used for preparing and running UPLC-MS and GC-MS samples.

Extraction

Rat cecal and human fecal samples (approximately 50 mg each) were collected in preweighed lysis tubes. The lysis tubes contained ceramic beads to allow for homogenization (Precellys lysing kit tough microorganism lysing VK05 tubes for rat cecal and human fecal samples; Bertin Technologies, Montigny-le-Bretonneux, France). Four hundred microliters of methanol (MeOH) was added to rat cecal and human feces, and the tubes were homogenized in a MagNA Lyser (6000 speed for 90 s and 7000 speed for 60 s). For portal venous samples, serum (100 μl) was collected in Eppendorf tubes, followed by addition of 100 μl of MeOH. Samples were vortexed and frozen at −20°C until further analysis. Cell culture medium was diluted 1:1 in MeOH.

All MeOH-extracted samples were centrifuged at 4°C for 30 min at 15,000 rpm. The supernatant was diluted 1:1 in 50% MeOH/water and centrifuged again at 4°C for 30 min at 15,000 rpm. The supernatant was transferred into mass spectrometry vials and injected into the UPLC-MS for BA analyses and the GC-MS for cholesterol analyses. Total BAs or cholesterol was then calculated by adding all detected and measured BAs. The limits of detection for individual BAs have been described previously (*40*, *49*, *62*).

Caco-2 cell culture and differentiation

Caco-2 cells were obtained from American Type Culture Collection (Manassas, VA). Cells were maintained in minimum essential medium with GlutaMAX and Earle's salts (Gibco, Life Technologies, UK). Cell culture media were supplemented with 10% fetal bovine serum (FBS), penicillin (100 U/ml), and streptomycin (100 μg/ml; GenClone). Cells were grown in FBS- and antibiotic-supplemented "complete" media at 37°C in an atmosphere of 5% CO_2. Undifferentiated Caco-2 cells were seeded in 24-well plate transwells (0.4-μM pore size, Costar) at 200,000 cells per transwell. Medium was changed on days 4, 8, 12, 16, and 18 to differentiate Caco-2 cells in vitro (*63*). On day 21, fully differentiated and polarized cells were used for permeability and toxicity assays.

H&E staining and light microscopy of transwells

Differentiated Caco-2 cells in transwells were stained with H&E stain (Abcam, ab245880) according to the manufacturer's instructions. Briefly, transwells were washed with PBS, followed by staining with hematoxylin for 5 min. Transwells were rinsed twice in distilled water (dH_2O) to remove excess stain, followed by the addition of bluing reagent and incubation for 10 to 15 s. Two rinses in dH_2O were performed before addition of ethanol (Sigma-Aldrich) to remove excess reagent. Ethanol was removed, and adequate eosin was added for 2 to 3 min for the counter stain. Transwells were dehydrated in ethanol two to three times, dried, and imaged using an EVOS XL Core microscope (Invitrogen) attached to camera at the ICCB-Longwood Screening Facility at HMS. Cells were imaged from the top, and all images were taken at the same magnification and light intensity. For each treatment, $n = 2$ transwells were imaged, providing four images per transwell. Representative images are shown in Figs. 2, 3, and 6.

In vitro BA treatments

Caco-2 cells (undifferentiated in 96-well plates or days 21 to 25 of differentiation in transwells) were treated with BA mixtures for 12 to 16 hours before assays. Unless otherwise specified, the compositions of the BA mixture used were the following: conjugated BAs represents equimolar concentrations of TβMCA, TCA, TDCA, TUDCA, TCDCA; unconjugated BAs represents equimolar concentrations of βMCA, CA, DCA, UDCA, CDCA; and combined BA pools represents equimolar concentrations of both pools. Diluted stocks of BA standards or undiluted methanol-extracted cecal contents were added in complete media. Transcytosis of BAs was measured by drying basolateral media in a SpeedVac, followed by resuspending the media in 1:1 methanol/water, transferred into mass spectrometry vials, and injected onto the UPLC-MS.

Caco-2 permeability assay

Epithelial integrity by FITC-dextran permeability assay was performed as previously described (*40*). Briefly, differentiated Caco-2 epithelial integrity was assayed by measuring passive diffusion of 4-kDa FITC-dextran (Sigma-Aldrich) added at a concentration of 5 μM to the apical chamber in 100 μl of PBS, while the basolateral chamber contained 500 μl of PBS. Diffusion from the apical to basolateral side was measured by fluorescence reading in PBS on the basolateral side of the transwell system using a SpectraMax M5 plate reader (Molecular Devices, San Jose, CA) at the ICCB-Longwood Screening Facility. Fluorescence reading was normalized to the control.

Caco-2 cell viability assay

Caco-2 (undifferentiated in 96-well plates or days 21 to 25 of differentiation in transwells) cell viability was measured using the 3-(4,5-dimethylthiazol-2-yl)-2,5-diphenyltetrazolium bromide (MTT) assay (Abcam, ab211091) according to the manufacturer's instructions. Cells were treated with compounds for 12 to 16 hours before viability determination. Briefly, cell culture medium was replaced with the MTT reagent and incubated for 3 hours at 37°C. Following incubation, the MTT reagent was replaced with the MTT solvent and incubated for 15 min, followed by analysis using a SpectraMax M5 plate reader (Molecular Devices, San Jose, CA) at the ICCB-Longwood Screening Facility at HMS. Absorbance reading at 690 nm, as a measure of viability, was normalized to the control.

Protein assays

Caco-2 cells were treated with pools of BAs that mimic the average physiological concentrations found in cecum of CDAHFD- and HFD-fed rats at 48-hour and 1-week time points for 20 min. Cells were lysed in cell lysis buffer (Cell Signaling Technology, #9803) with protease inhibitor cocktail cOmplete Mini (Roche) and PhosSTOP (Roche). Lysates from rat ileum or cecum tissues were extracted using radioimmunoprecipitation assay buffer (Boston Bioproducts, Worcester, MA). Proteins were separated by gel electrophoresis performed using NuPAGE Bis-Tris Midi Gels (Thermo Fisher Scientific, Waltham, MA) for rat tissues and Mini-Protein TGX gels (Bio-Rad) for tissue culture lysates. Proteins were transferred to polyvinylidene difluoride membranes followed by blocking with 5% nonfat dry milk for 1 hour. The membranes were then incubated with primary antibodies overnight at 4°C and with secondary antibodies for 1 hour at room temperature. The following antibodies were used: apical sodium bile acid transporter (ASBT) (#ab203205, Abcam, Waltham, MA), organic solute transporter α (OSTα) (#NBP1-57085, Novus Biologicals, Littleton, CO), OST beta (OSTβ) (#BS-2128R, Bioss Antibodies, Woburn, MA), Takeda G protein-coupled receptor (TGR5) (#PA5-77294, Thermo Fisher Scientific), glyceraldehyde-3-phosphate dehydrogenase (GAPDH) (#2118, Cell Signaling Technology, Beverly, MA), α-actin (#8457, Cell Signaling Technology), phosphorylated EGFR (pEGFR) (#3777, Cell Signaling Technology), tubulin (#2125, Cell Signaling Technology), and anti-rabbit immunoglobulin G horseradish peroxidase (HRP) (#7074, Cell Signaling Technology). The blots were developed by a HRP system using ChemiDoc (Bio-Rad Laboratories, Hercules, CA) and quantified using Image Lab software (Bio-Rad Laboratories).

CMC assay

CMC determination of groups of BAs with or without lecithin and cholesterol was performed using a previously described assay using coumarin 6 as a fluorescent probe with minor adaptations (*43*). Briefly, 6 mM coumarin 6 (Sigma-Aldrich) in dichloromethane (Sigma-Aldrich) was added to Eppendorf tubes and allowed to evaporate for 30 min in a chemical hood. Equimolar mixtures (400 μl)

of BAs at various concentrations to be tested were added to tubes and rotated overnight at room temperature in the dark [unconjugated BAs: βMCA, CA, CDCA, UDCA, and DCA; tauro-conjugated BAs: TβMCA, TCA, TCDCA, TUDCA, and TDCA; and glyco-conjugated BAs: GCA, GDCA, GUDCA, GCDCA, lecithin (1 mM), and cholesterol (150 μM)]. The next day, 200 μl of the solution was transferred to black 96-well plates (Costar), and fluorescence intensity at 480/530 was measured using a SpectraMax M5 plate reader (Molecular Devices, San Jose, CA) at the ICCB-Longwood Screening Facility. Fluorescence intensity was plotted against the logarithm of the corresponding concentration, and the CMC was determined by the intersection of the two tangents created in the graph.

Electron microscopy

Caco-2 cells seeded on transwells were washed in PBS before fixation in FGOP (formaldehyde-glutaraldehyde-picric acid) fixative. Samples were fixed overnight in a mixture of 1.25% formaldehyde, 2.5% glutaraldehyde, and 0.03% picric acid in 0.1 M sodium cacodylate buffer, (pH 7.4). FGOP fixative was diluted in 1:1 PBS before applying to the apical and basolateral chamber of transwells. Fixed samples were stored at 4°C until further processing and imaging by the Electron Microscopy Core at HMS. All EM imaging was performed by a blinded investigator.

For TEM, fixed tissues were washed with 0.1 M sodium cacodylate buffer and postfixed with 1% osmium tetroxide/1.5% potassium ferrocyanide (in H_2O) for 2 hours. Samples were then washed in a maleate buffer and postfixed in 1% uranyl acetate in maleate buffer for 1 hour. Tissues were then rinsed in double-distilled H_2O and dehydrated through a series of ethanol [50, 70, 95, and (2×) 100%] for 15 min per solution. Dehydrated tissues were put in propylene oxide for 5 min before they were infiltrated in 1:1 epon mixed with propylene oxide overnight at 4°C. Samples were polymerized in a 60°C oven in epon resin for 48 hours. They were then sectioned into 80-nm-thin sections and imaged on a JEOL 1200EX TEM.

For negative staining for visualization of micelles, the sample was diluted in water and adsorbed onto a glow-discharged carbon grid. Once the specimen was adsorbed on to the film surface, the excess liquid was blotted off using a filter paper (Whatman #1), and the grid was floated on a small drop (~5 μl) of staining solution (0.75% uranyl acetate). After 20 s, the excess stain was blotted off, and the sample was air-dried briefly before it was examined in the TEM.

BSH activity assay

BSH activity was quantified using a modified version of a previously described method (*27*). Briefly, fresh cecal contents (approximately 20 mg) were diluted in PBS to obtain a concentration of 1 mg/ml, and 100 μM GCFCA-d4 was added to the mixture and incubated at 37°C for 30 min, then frozen in dry ice for 5 min, and stored at −80°C until further analysis. On thawing, the mixture was diluted with an equal volume of methanol, and the slurry was centrifuged at 12,500*g* for 10 min. The supernatant was removed into a clean Eppendorf tube and centrifuged again. The supernatant was transferred to mass spectrometry vials, and samples were analyzed as described in BA analysis in the Supplementary Materials.

Statistical analyses

Data were quantified using software linked to indicated instruments and plotted in GraphPad Prism 7. Statistical analyses were performed using GraphPad Prism and Microsoft Excel software. Statistical significance was assessed using Student's or Welch's *t* tests, one-way or two-way analyses of variance (ANOVAs) followed by multiple comparisons tests, and Mann-Whitney tests wherever appropriate. In Figs. 1 (E and F) and 4G, and fig. S18, intestines from all animals were stained; $n = 10$ intestinal cell images per group were analyzed. For ZO-1 intensity, one-way ANOVA followed by Tukey's multiple comparisons test was used, and for %ZO-1 membrane intensity and 4′,6-diamidino-2-phenylindole (DAPI) intensity, two-tailed Welch's *t* test was used. In Fig. 2 (A and B), one-way ANOVA followed by Dunnett's multiple comparisons test was used for treatment versus DMSO, and one-way ANOVA followed by Tukey's multiple comparisons test was used for comparing treatments. In Figs. 2 (E and F), 3 (E, G, and H), and 6 (F and H), two-way ANOVA followed by Sidak's multiple comparisons test was used.

Ethics

Animals received humane care per criteria outlined in the Guide for the Care and Use of Laboratory Animals by the National Academy of Sciences (National Institutes of Health publication 86-23, revised 1985) and in accordance with the Massachusetts General Hospital Institutional Animal Care and Use Committee guidelines (Protocol 2007 N000113).

SUPPLEMENTARY MATERIALS

Supplementary material for this article is available at https://science.org/doi/10.1126/sciadv.abo2794

View/request a protocol for this paper from *Bio-protocol*.

REFERENCES AND NOTES

1. A. Buckley, J. R. Turner, Cell biology of tight junction barrier regulation and mucosal disease. *Cold Spring Harb. Perspect. Biol.* **10**, ea029314 (2018).
2. L. Massier, M. Bluher, P. Kovacs, R. M. Chakaroun, Impaired intestinal barrier and tissue bacteria: Pathomechanisms for metabolic diseases. *Front. Endocrinol. (Lausanne)* **12**, 616506 (2021).
3. E. Bosi, L. Molteni, M. G. Radaelli, L. Folini, I. Fermo, E. Bazzigaluppi, L. Piemonti, M. R. Pastore, R. Paroni, Increased intestinal permeability precedes clinical onset of type 1 diabetes. *Diabetologia* **49**, 2824–2827 (2006).
4. D. M. Chopyk, A. Grakoui, Contribution of the intestinal microbiome and gut barrier to hepatic disorders. *Gastroenterology* **159**, 849–863 (2020).
5. A. Damms-Machado, S. Louis, A. Schnitzer, V. Volynets, A. Rings, M. Basrai, S. C. Bischoff, Gut permeability is related to body weight, fatty liver disease, and insulin resistance in obese individuals undergoing weight reduction. *Am. J. Clin. Nutr.* **105**, 127–135 (2017).
6. L. Ohlsson, A. Gustafsson, E. Lavant, K. Suneson, L. Brundin, A. Westrin, L. Ljunggren, D. Lindqvist, Leaky gut biomarkers in depression and suicidal behavior. *Acta Psychiatr. Scand.* **139**, 185–193 (2019).
7. E. Pasini, R. Aquilani, C. Testa, P. Baiardi, S. Angioletti, F. Boschi, M. Verri, F. Dioguardi, Pathogenic gut flora in patients with chronic heart failure. *JACC Heart Fail* **4**, 220–227 (2016).
8. A. Albillos, A. de Gottardi, M. Rescigno, The gut-liver axis in liver disease: Pathophysiological basis for therapy. *J. Hepatol.* **72**, 558–577 (2020).
9. R. M. Chakaroun, L. Massier, P. Kovacs, Gut microbiome, intestinal permeability, and tissue bacteria in metabolic disease: Perpetrators or bystanders? *Nutrients* **12**, 1082 (2020).
10. Y. Murakami, S. Tanabe, T. Suzuki, High-fat diet-induced intestinal hyperpermeability is associated with increased bile acids in the large intestine of Mice. *J. Food Sci.* **81**, H216–H222 (2016).
11. S. C. Papillon, M. R. Frey, H. R. Ford, C. P. Gayer, Secondary bile acids as a mechanism of intestinal injury. *J. Am. Coll. Surg.* **217**, S13 (2013).
12. J. P. Hamilton, G. Xie, J. P. Raufman, S. Hogan, T. L. Griffin, C. A. Packard, D. A. Chatfield, L. R. Hagey, J. H. Steinbach, A. F. Hofmann, Human cecal bile acids: Concentration and spectrum. *Am. J. Physiol. Gastrointest. Liver Physiol.* **293**, G256–G263 (2007).
13. T. Q. de Aguiar Vallim, E. J. Tarling, P. A. Edwards, Pleiotropic roles of bile acids in metabolism. *Cell Metab.* **17**, 657–669 (2013).
14. J. M. Ridlon, S. C. Harris, S. Bhowmik, D. J. Kang, P. B. Hylemon, Consequences of bile salt biotransformations by intestinal bacteria. *Gut Microbes* **7**, 22–39 (2016).
15. Z. Song, Y. Cai, X. Lao, X. Wang, X. Lin, Y. Cui, P. K. Kalavagunta, J. Liao, L. Jin, J. Shang, J. Li, Taxonomic profiling and populational patterns of bacterial bile salt hydrolase (BSH) genes based on worldwide human gut microbiome. *Microbiome* **7**, 9 (2019).

16. M. H. Foley, S. O'Flaherty, R. Barrangou, C. M. Theriot, Bile salt hydrolases: Gatekeepers of bile acid metabolism and host-microbiome crosstalk in the gastrointestinal tract. *PLOS Pathog.* **15**, e1007581 (2019).
17. J. C. Poland, C. R. Flynn, Bile acids, their receptors, and the gut microbiota. *Physiology (Bethesda)* **36**, 235–245 (2021).
18. A. Di Ciaula, G. Garruti, R. Lunardi Baccetto, E. Molina-Molina, L. Bonfrate, D. Q. Wang, P. Portincasa, Bile acid physiology. *Ann. Hepatol.* **16**, S4–S14 (2017).
19. F. Raimondi, P. Santoro, M. V. Barone, S. Pappacoda, M. L. Barretta, M. Nanayakkara, C. Apicella, L. Capasso, R. Paludetto, Bile acids modulate tight junction structure and barrier function of Caco-2 monolayers via EGFR activation. *Am. J. Physiol. Gastrointest. Liver Physiol.* **294**, G906–G913 (2008).
20. J. Sarathy, S. J. Detloff, M. Ao, N. Khan, S. French, H. Sirajuddin, T. Nair, M. C. Rao, The Yin and Yang of bile acid action on tight junctions in a model colonic epithelium. *Physiol. Rep.* **5**, e13294 (2017).
21. L. K. Stenman, R. Holma, R. Korpela, High-fat-induced intestinal permeability dysfunction associated with altered fecal bile acids. *World J. Gastroenterol.* **18**, 923–929 (2012).
22. L. K. Stenman, R. Holma, A. Eggert, R. Korpela, A novel mechanism for gut barrier dysfunction by dietary fat: Epithelial disruption by hydrophobic bile acids. *Am. J. Physiol. Gastrointest. Liver Physiol.* **304**, G227–G234 (2013).
23. B. Gupta, Y. Liu, D. M. Chopyk, R. P. Rai, C. Desai, P. Kumar, A. B. Farris, A. Nusrat, C. A. Parkos, F. A. Anania, R. Raeman, Western diet-induced increase in colonic bile acids compromises epithelial barrier in nonalcoholic steatohepatitis. *FASEB J.* **34**, 7089–7102 (2020).
24. A. Nicoletti, F. R. Ponziani, M. Biolato, V. Valenza, G. Marrone, G. Sganga, A. Gasbarrini, L. Miele, A. Grieco, Intestinal permeability in the pathogenesis of liver damage: From non-alcoholic fatty liver disease to liver transplantation. *World J. Gastroenterol.* **25**, 4814–4834 (2019).
25. L. Longo, J. T. Ferrari, P. H. Rampelotto, G. H. Dellavia, A. Pasqualotto, C. P. Oliveira, C. T. S. Cerski, T. R. da Silveira, C. Uribe-Cruz, M. R. Álvares-da-Silva, Gut dysbiosis and increased intestinal permeability drive microRNAs, NLRP-3 inflammasome and liver fibrosis in a nutritional model of non-alcoholic steatohepatitis in adult male sprague dawley rats. *Clin. Exp. Gastroenterol.* **13**, 351–368 (2020).
26. A. A. Adhikari, D. Ramachandran, S. N. Chaudhari, C. E. Powell, M. D. McCurry, A. S. Banks, A. S. Devlin, A gut-restricted lithocholic acid analog as an inhibitor of gut bacterial bile salt hydrolases. *ACS Chem. Biol.* **16**, 1401–1412 (2021).
27. A. A. Adhikari, T. C. M. Seegar, S. B. Ficarro, M. D. McCurry, D. Ramachandran, L. Yao, S. N. Chaudhari, S. Ndousse-Fetter, A. S. Banks, J. A. Marto, S. C. Blacklow, A. S. Devlin, Development of a covalent inhibitor of gut bacterial bile salt hydrolases. *Nat. Chem. Biol.* **16**, 318–326 (2020).
28. F. Zhong, X. Zhou, J. Xu, L. Gao, Rodent models of nonalcoholic fatty liver disease. *Digestion* **101**, 522–535 (2020).
29. K. D. Corbin, S. H. Zeisel, Choline metabolism provides novel insights into nonalcoholic fatty liver disease and its progression. *Curr. Opin. Gastroenterol.* **28**, 159–165 (2012).
30. A. L. Guerrerio, R. M. Colvin, A. K. Schwartz, J. P. Molleston, K. F. Murray, A. Diehl, P. Mohan, J. B. Schwimmer, J. E. Lavine, M. S. Torbenson, A. O. Scheimann, Choline intake in a large cohort of patients with nonalcoholic fatty liver disease. *Am. J. Clin. Nutr.* **95**, 892–900 (2012).
31. M. Matsumoto, N. Hada, Y. Sakamaki, A. Uno, T. Shiga, C. Tanaka, T. Ito, A. Katsume, M. Sudoh, An improved mouse model that rapidly develops fibrosis in non-alcoholic steatohepatitis. *Int. J. Exp. Pathol.* **94**, 93–103 (2013).
32. W. Guo, P. Wang, Z. H. Liu, P. Ye, Analysis of differential expression of tight junction proteins in cultured oral epithelial cells altered by Porphyromonas gingivalis, Porphyromonas gingivalis lipopolysaccharide, and extracellular adenosine triphosphate. *Int. J. Oral Sci.* **10**, e8 (2018).
33. J. Karczewski, F. J. Troost, I. Konings, J. Dekker, M. Kleerebezem, R. J. Brummer, J. M. Wells, Regulation of human epithelial tight junction proteins by Lactobacillus plantarum in vivo and protective effects on the epithelial barrier. *Am. J. Physiol. Gastrointest. Liver Physiol.* **298**, G851–G859 (2010).
34. Y. Guan, A. J. Watson, A. M. Marchiando, E. Bradford, L. Shen, J. R. Turner, M. H. Montrose, Redistribution of the tight junction protein ZO-1 during physiological shedding of mouse intestinal epithelial cells. *Am. J. Physiol. Cell Physiol.* **300**, C1404–C1414 (2011).
35. M. A. Odenwald, W. Choi, A. Buckley, N. Shashikanth, N. E. Joseph, Y. Wang, M. H. Warren, M. M. Buschmann, R. Pavlyuk, J. Hildebrand, B. Margolis, A. S. Fanning, J. R. Turner, ZO-1 interactions with F-actin and occludin direct epithelial polarization and single lumen specification in 3D culture. *J. Cell Sci.* **130**, 243–259 (2017).
36. J. P. Arab, S. J. Karpen, P. A. Dawson, M. Arrese, M. Trauner, Bile acids and nonalcoholic fatty liver disease: Molecular insights and therapeutic perspectives. *Hepatology* **65**, 350–362 (2017).
37. F. Li, C. Jiang, K. W. Krausz, Y. Li, I. Albert, H. Hao, K. M. Fabre, J. B. Mitchell, A. D. Patterson, F. J. Gonzalez, Microbiome remodelling leads to inhibition of intestinal farnesoid X receptor signalling and decreased obesity. *Nat. Commun.* **4**, 2384 (2013).
38. S. Fiorucci, E. Distrutti, Bile acid-activated receptors, intestinal microbiota, and the treatment of metabolic disorders. *Trends Mol. Med.* **21**, 702–714 (2015).
39. S. A. Scott, J. Fu, P. V. Chang, Microbial tryptophan metabolites regulate gut barrier function via the aryl hydrocarbon receptor. *Proc. Natl. Acad. Sci. U.S.A.* **117**, 19376–19387 (2020).
40. S. N. Chaudhari, D. A. Harris, H. Aliakbarian, J. N. Luo, M. T. Henke, R. Subramaniam, A. H. Vernon, A. Tavakkoli, E. G. Sheu, A. S. Devlin, Bariatric surgery reveals a gut-restricted TGR5 agonist with anti-diabetic effects. *Nat. Chem. Biol.* **17**, 20–29 (2021).
41. J. D. Soderholm, G. Olaison, K. H. Peterson, L. E. Franzen, T. Lindmark, M. Wiren, C. Tagesson, R. Sjodahl, Augmented increase in tight junction permeability by luminal stimuli in the non-inflamed ileum of Crohn's disease. *Gut* **50**, 307–313 (2002).
42. A. F. Hofmann, The function of bile salts in fat absorption. the solvent properties of dilute micellar solutions of conjugated bile salts. *Biochem. J.* **89**, 57–68 (1963).
43. A. Fluksman, O. Benny, A robust method for critical micelle concentration determination using coumarin-6 as a fluorescent probe. *Anal. Methods* **11**, 3810–3818 (2019).
44. N. Pavlovic, S. Golocorbin-Kon, M. Đanić, B. Stanimirov, H. Al-Salami, K. Stankov, M. Mikov, Bile acids and their derivatives as potential modifiers of drug release and pharmacokinetic profiles. *Front. Pharmacol.* **9**, 1283 (2018).
45. J. M. Donovan, N. Timofeyeva, M. C. Carey, Influence of total lipid concentration, bile salt: Lecithin ratio, and cholesterol content on inter-mixed micellar/vesicular (non-lecithin-associated) bile salt concentrations in model bile. *J. Lipid Res.* **32**, 1501–1512 (1991).
46. D. Jungst, T. Lang, P. Huber, V. Lange, G. Paumgartner, Effect of phospholipids and bile acids on cholesterol nucleation time and vesicular/micellar cholesterol in gallbladder bile of patients with cholesterol stones. *J. Lipid Res.* **34**, 1457–1464 (1993).
47. D. Dahlgren, M. Venczel, J. P. Ridoux, C. Skjold, A. Mullertz, R. Holm, P. Augustijns, P. M. Hellstrom, H. Lennernas, Fasted and fed state human duodenal fluids: Characterization, drug solubility, and comparison to simulated fluids and with human bioavailability. *Eur. J. Pharm. Biopharm.* **163**, 240–251 (2021).
48. Z. Zhou, C. Dunn, I. Khadra, C. G. Wilson, G. W. Halbert, Influence of physiological gastrointestinal surfactant ratio on the equilibrium solubility of BCS class II drugs investigated using a four component mixture design. *Mol. Pharm.* **14**, 4132–4144 (2017).
49. L. Yao, S. C. Seaton, S. Ndousse-Fetter, A. A. Adhikari, N. DiBenedetto, A. I. Mina, A. S. Banks, L. Bry, A. S. Devlin, A selective gut bacterial bile salt hydrolase alters host metabolism. *eLife* **7**, e37182 (2018).
50. J. Boursier, O. Mueller, M. Barret, M. Machado, L. Fizanne, F. Araujo-Perez, C. D. Guy, P. C. Seed, J. F. Rawls, L. A. David, G. Hunault, F. Oberti, P. Cales, A. M. Diehl, The severity of nonalcoholic fatty liver disease is associated with gut dysbiosis and shift in the metabolic function of the gut microbiota. *Hepatology* **63**, 764–775 (2016).
51. R. Loomba, V. Seguritan, W. Li, T. Long, N. Klitgord, A. Bhatt, P. S. Dulai, C. Caussy, R. Bettencourt, S. K. Highlander, M. B. Jones, C. B. Sirlin, B. Schnabl, L. Brinkac, N. Schork, C. H. Chen, D. A. Brenner, W. Biggs, S. Yooseph, J. C. Venter, K. E. Nelson, Gut microbiome-based metagenomic signature for non-invasive detection of advanced fibrosis in human nonalcoholic fatty liver disease. *Cell Metab.* **30**, 607 (2019).
52. M. Mouzaki, A. Y. Wang, R. Bandsma, E. M. Comelli, B. M. Arendt, L. Zhang, S. Fung, S. E. Fischer, I. G. McGilvray, J. P. Allard, Bile acids and dysbiosis in non-alcoholic fatty liver disease. *PLOS ONE* **11**, e0151829 (2016).
53. N. Nimer, I. Choucair, Z. Wang, I. Nemet, L. Li, J. Gukasyan, T. L. Weeks, N. Alkhouri, N. Zein, W. H. W. Tang, M. A. Fischbach, J. M. Brown, H. Allayee, S. Dasarathy, V. Gogonea, S. L. Hazen, Bile acids profile, histopathological indices and genetic variants for non-alcoholic fatty liver disease progression. *Metabolism* **116**, 154457 (2021).
54. P. Puri, K. Daita, A. Joyce, F. Mirshahi, P. K. Santhekadur, S. Cazanave, V. A. Luketic, M. S. Siddiqui, S. Boyett, H. K. Min, D. P. Kumar, R. Kohli, H. Zhou, P. B. Hylemon, M. J. Contos, M. Idowu, A. J. Sanyal, The presence and severity of nonalcoholic steatohepatitis is associated with specific changes in circulating bile acids. *Hepatology* **67**, 534–548 (2018).
55. P. Hegyi, J. Maleth, J. R. Walters, A. F. Hofmann, S. J. Keely, Guts and gall: Bile acids in regulation of intestinal epithelial function in health and disease. *Physiol. Rev.* **98**, 1983–2023 (2018).
56. Y. Araki, A. Andoh, H. Bamba, K. Yoshikawa, H. Doi, Y. Komai, A. Higuchi, Y. Fujiyama, The cytotoxicity of hydrophobic bile acids is ameliorated by more hydrophilic bile acids in intestinal cell lines IEC-6 and Caco-2. *Oncol. Rep.* **10**, 1931–1936 (2003).
57. A. Di Ciaula, D. Q. Wang, E. Molina-Molina, R. Lunardi Baccetto, G. Calamita, V. O. Palmieri, P. Portincasa, Bile acids and cancer: Direct and environmental-dependent effects. *Ann. Hepatol.* **16**, S87–S105 (2017).
58. A. F. Hofmann, Bile acids: The good, the bad, and the ugly. *News Physiol. Sci.* **14**, 24–29 (1999).
59. K. Brandl, B. Schnabl, Intestinal microbiota and nonalcoholic steatohepatitis. *Curr. Opin. Gastroenterol.* **33**, 128–133 (2017).
60. A. Woting, M. Blaut, Small intestinal permeability and gut-transit time determined with low and high molecular weight fluorescein isothiocyanate-dextrans in C_3H mice. *Nutrients* **10**, 685 (2018).

61. P. R. Hutson, M. E. Crawford, R. L. Sorkness, Liquid chromatographic determination of hydroxyproline in tissue samples. *J. Chromatogr. B Analyt. Technol. Biomed. Life Sci.* **791**, 427–430 (2003).
62. S. N. Chaudhari, J. N. Luo, D. A. Harris, H. Aliakbarian, L. Yao, D. Paik, R. Subramaniam, A. A. Adhikari, A. H. Vernon, A. Kilic, S. T. Weiss, J. R. Huh, E. G. Sheu, A. S. Devlin, A microbial metabolite remodels the gut-liver axis following bariatric surgery. *Cell Host Microbe* **29**, 408–424.e7 (2021).
63. T. Lea, "Caco-2 Cell Line" in *The Impact of Food Bioactives on Health: In vitro and ex vivo models*, K. Verhoeckx, P. Cotter, I. Lopez-Exposito, C. Kleiveland, T. Lea, A. Mackie, T. Requena, D. Swiatecka, H. Wichers, Eds. (Springer, 2015), pp. 103–111.
64. M. C. Carey, D. M. Small, Micelle formation by bile salts. Physical-chemical and thermodynamic considerations. *Arch. Intern. Med.* **130**, 506–527 (1972).
65. S. Faramarzi, B. Bonnett, C. A. Scaggs, A. Hoffmaster, D. Grodi, E. Harvey, B. Mertz, Molecular dynamics simulations as a tool for accurate determination of surfactant micelle properties. *Langmuir* **33**, 9934–9943 (2017).

Acknowledgments: We are indebted to members of the Devlin, Chung, and Tanabe groups for helpful discussions. We thank the HMS Electron Microscopy core for technical support and advice. We are grateful to the human patients who participated in this study. **Funding:** The research was supported by National Institutes of Health (NIH) grant R35 GM128618 (to A.S.D.), an Innovation Award from the Center for Microbiome Informatics and Therapeutics at MIT (to A.S.D), a grant from Harvard Digestive Diseases Center (supported by NIH grant 5P30DK034854-32) (to A.S.D), a Quadrangle Fund for the Advancement and Seeding of Translational Research at HMS (Q-FASTR) grant (to A.S.D. and R.T.C.), and the MGH Research Scholars Program (to R.T.C.). D.K.L. was supported by NIH T32 training grant (5T32DK007191). S.N.C. acknowledges an American Heart Association Postdoctoral Fellowship and an NIH K99/R00 Pathway to Independence Award (K99 DK128503). The rat images in the figures were provided by BioRender. **Author contributions:** D.K.L., S.N.C., R.T.C., and A.S.D. conceived the project and designed the experiments. D.K.L., M.S., Y.L., and S.C.B. performed all animal experiments, immunofluorescence, staining, and transcriptional analyses on rat tissues. S.N.C. performed the cell culture experiments, BA profiling, and preparation for EM. S.S. and L.Z. performed pathology scoring of rat tissue. D.K.L., S.N.C., and A.S.D. wrote the manuscript. All authors edited and contributed to the critical review of the manuscript. **Competing interests:** A.S.D. is an ad hoc consultant for Takeda Pharmaceuticals and Axial Therapeutics. A.S.D. and A.A.A. are inventors on a patent application related to this work filed by the President and Fellows of Harvard College (no. PCT/US2020/032016, filed 8 May 2020, published 19 November 2020). The other authors declare that they have no competing interests. **Data and materials availability:** All data needed to evaluate the conclusions in the paper are present in the paper and/or the Supplementary Materials. AAA-10 can be provided by the Devlin laboratory pending scientific review and a completed material transfer agreement. Requests for AAA-10 should be submitted to A.S.D.

Submitted 24 January 2022
Accepted 13 July 2022
Published 26 August 2022
10.1126/sciadv.abo2794